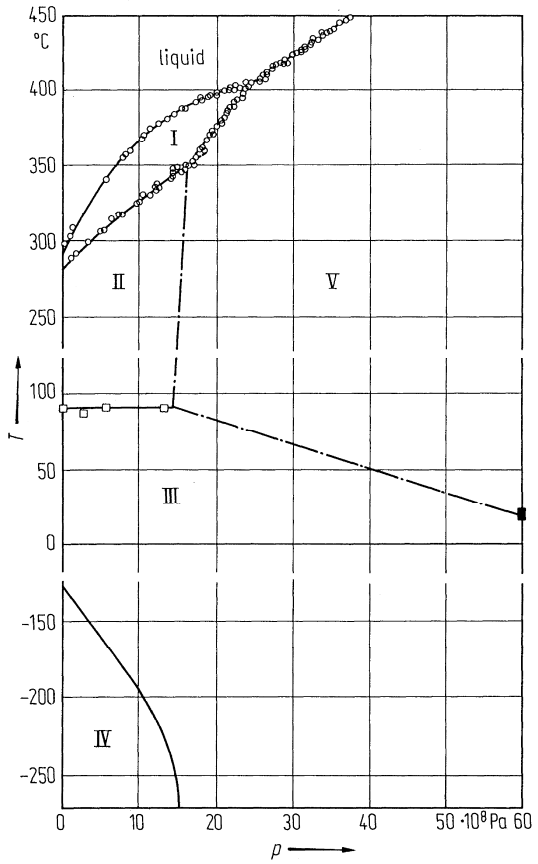

Fig. 33A-2-001. RbH_2PO_4 (RDP). Phase diagram [78Rap]. Open squares: quasi-irreversible transition. Full square: [69Bli3]. The IV–III phase boundary is from [73Pee]. Dashed-dotted line: tentative boundaries.

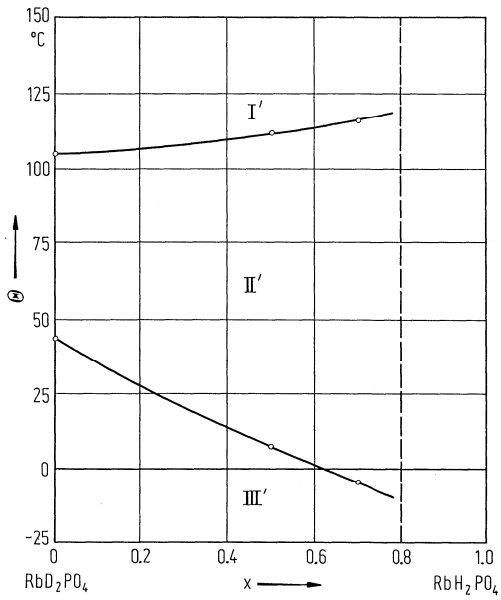

Fig. 33A-2-002. $RbD_{2(1-x)}H_{2x}PO_4$ (monoclinic). Θ vs. x [82Sum].

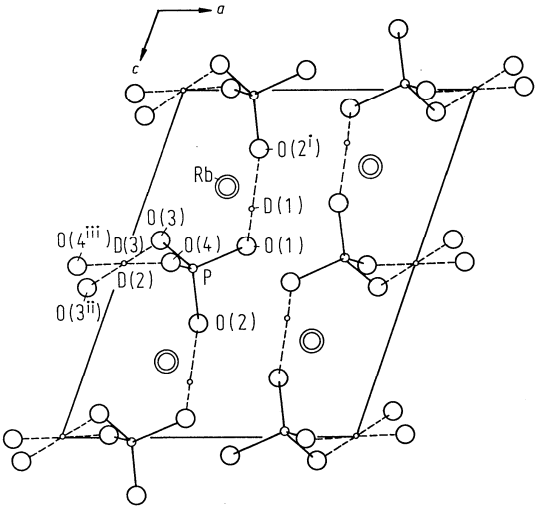

Fig. 33A-2-003. RbD_2PO_4 (monoclinic). Crystal structure of phase II′ [84Hag]. *b* projection. See Table 33A-2-010 for symmetry codes.

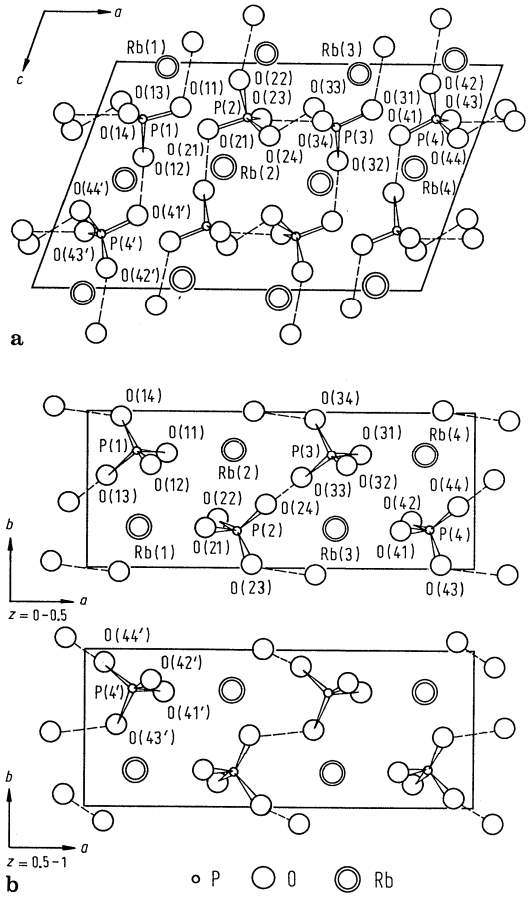

Fig. 33A-2-004. RbD_2PO_4 (monoclinic). Crystal structure of phase III′ [83Suz]. See Table 33A-2-011.

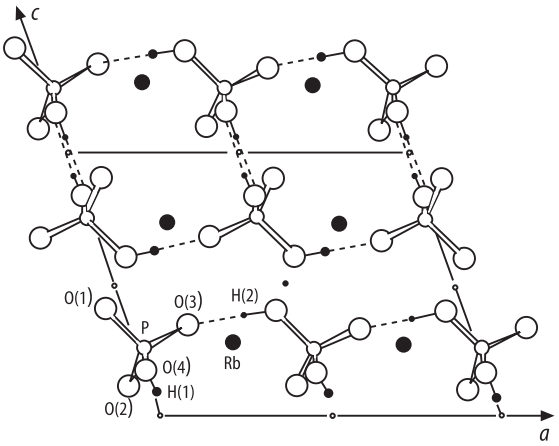

Fig. 33A-2-005. RbH_2PO_4 (RDP). Crystal structure of phase II [85Ave]. *b* projection.

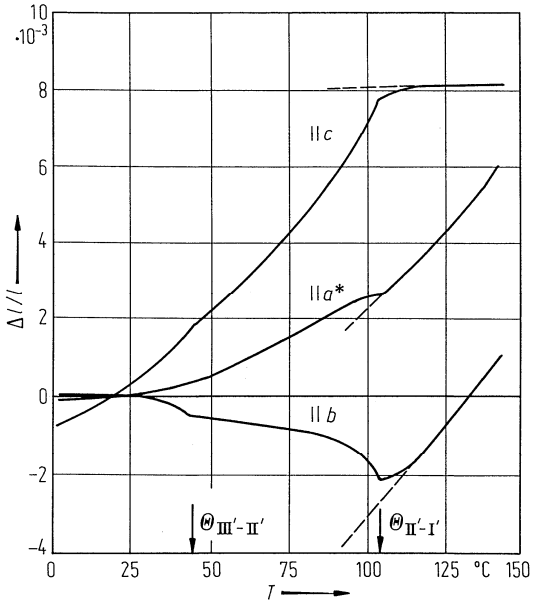

Fig. 33A-2-006. RbD_2PO_4 (monoclinic). $\Delta l/l$ vs. T [81Sum]. $\Delta l/l$: linear thermal expansion.

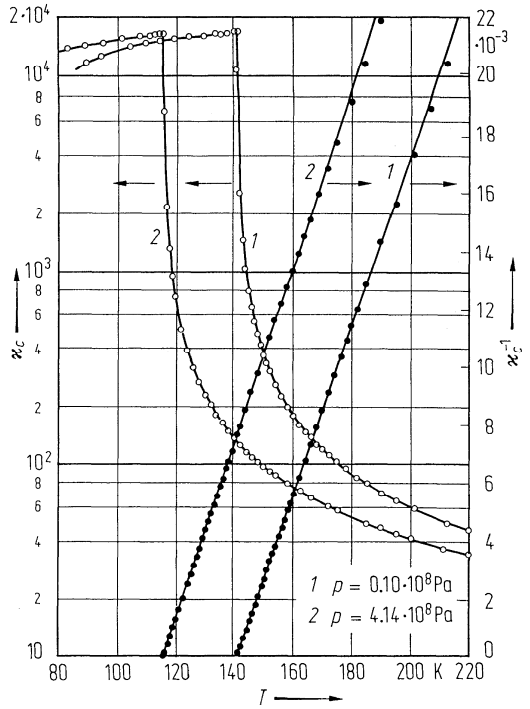

Fig. 33A-2-007. RbH_2PO_4 (RDP). κ_c, κ_c^{-1} vs. T [73Pee]. Parameter: p. f = 1 kHz.

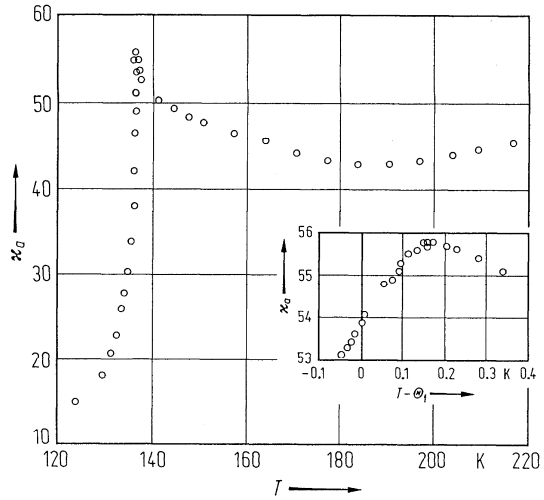

Fig. 33A-2-008. RbH_2PO_4 (RDP). κ_a vs. T [76Sin]. f = 1.596 kHz.

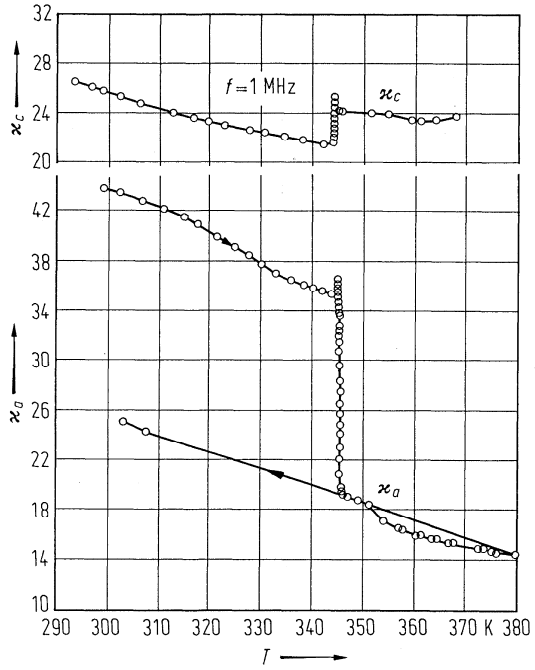

Fig. 33A-2-009. RbH_2PO_4 (RDP). κ_a, κ_c vs. T in the neighbourhood of Θ_{III-II} [78Sha].

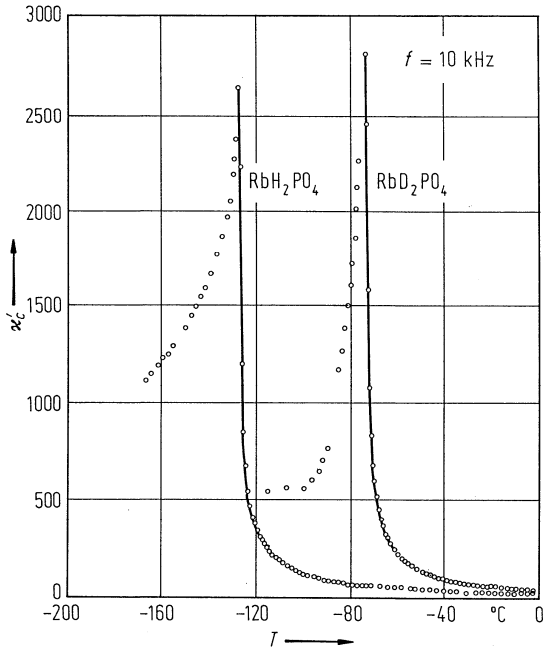

Fig. 33A-2-010. RbH_2PO_4 (RDP, tetragonal), RbD_2PO_4 (DRDP, tetragonal). κ_c vs. T [81Sum].

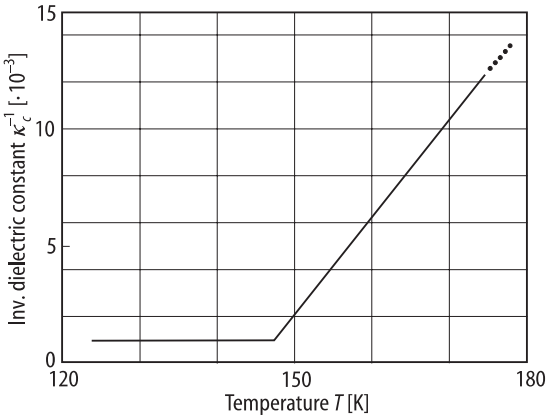

Fig. 33A-2-011. RbH_2PO_4 (RDP). κ_c^{-1} vs. T [85Mar]. f = 1 kHz. Applied ac voltage: 1 V rms.

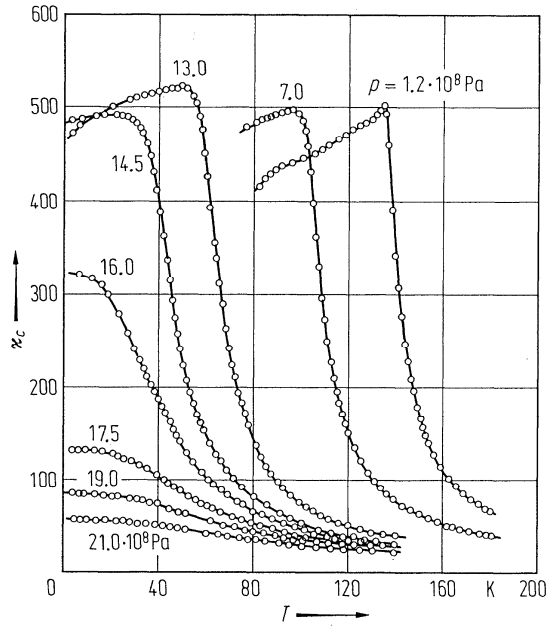

Fig. 33A-2-012. RbH_2PO_4 (RDP). $\varkappa_c$ vs. T [73Pee]. Parameter: p. f = 1 kHz.

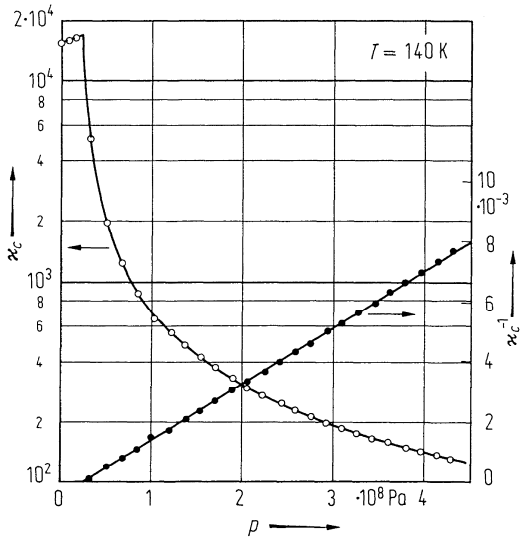

Fig. 33A-2-013. RbH_2PO_4 (RDP). κ_c, κ_c^{-1} vs. p at 140 K [73Pee]. f = 1 kHz.

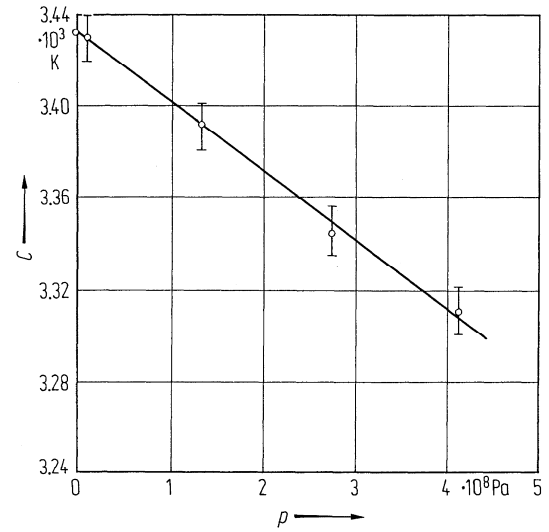

Fig. 33A-2-014. RbH_2PO_4 (RDP). C vs. p [73Pee]. C: Curie-Weiss constant.

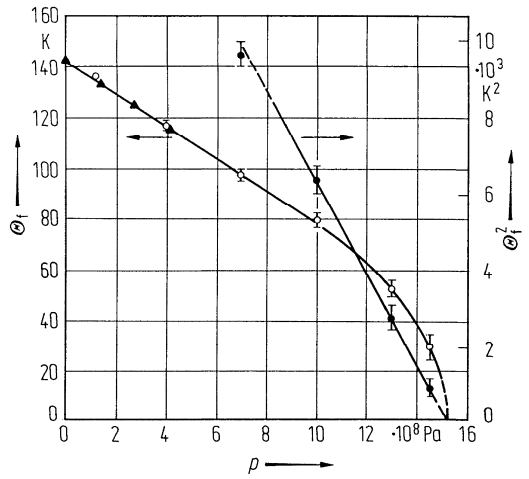

Fig. 33A-2-015. RbH_2PO_4 (RDP). Θ_f, Θ_f^2 vs. p [73Pee].

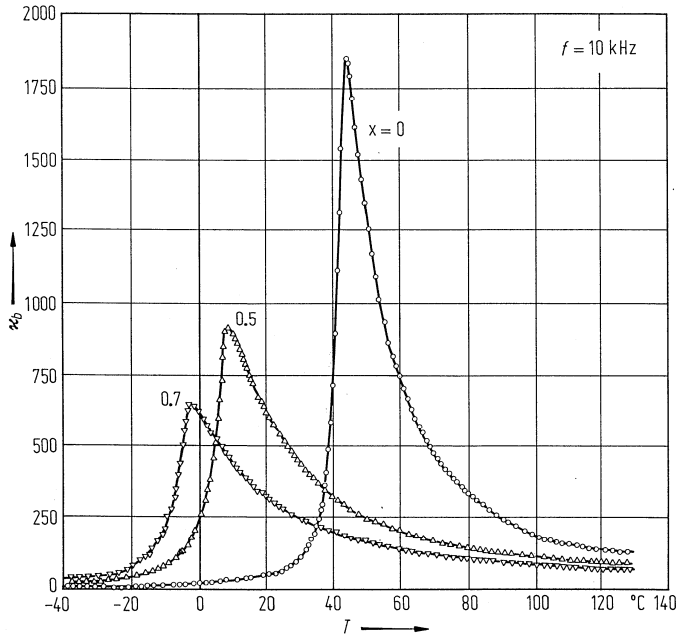

Fig. 33A-2-016. $RbD_{2(1-x)}H_{2x}PO_4$ (monoclinic). κ_b vs. T [82Sum]. Parameter: x.

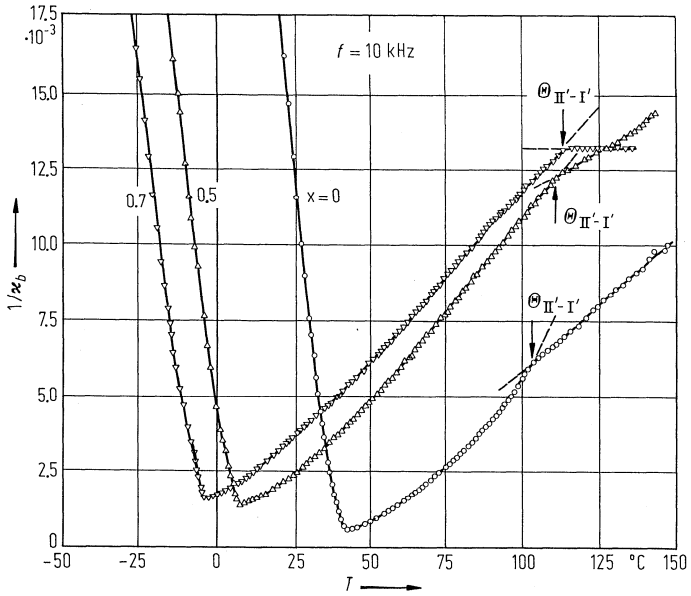

Fig. 33A-2-017. $RbD_{2(1-x)}H_{2x}PO_4$ (monoclinic). κ_b^{-1} vs. T [82Sum]. Parameter: x.

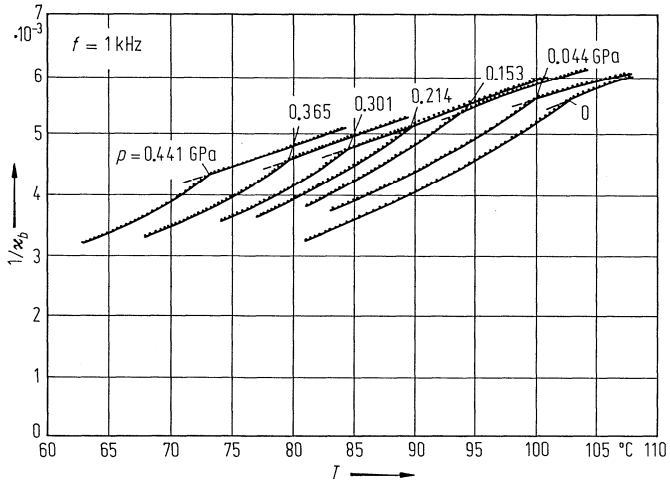

Fig. 33A-2-018. RbD_2PO_4 (monoclinic). κ_b^{-1} vs. T in the vicinity of $\Theta_{II'-I'}$ [83Ges]. Parameter: p.

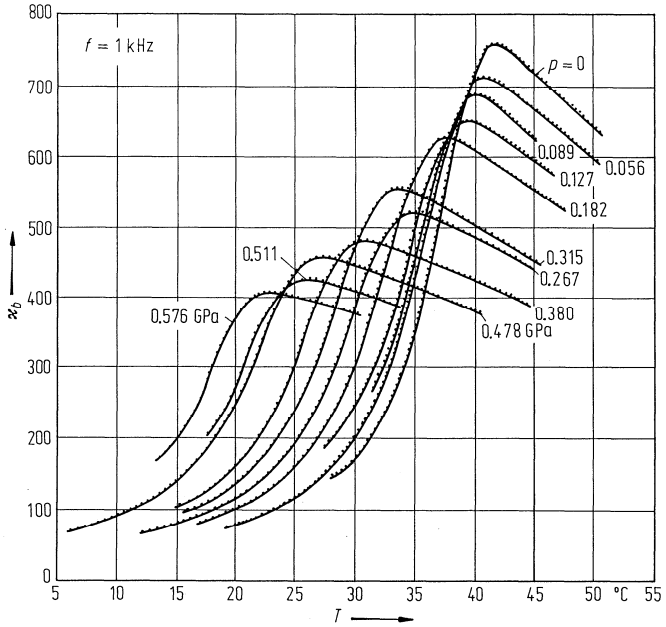

Fig. 33A-2-019. RbD_2PO_4 (monoclinic). κ_b vs. T near $\Theta_{III'-II'}$ [83Ges]. Parameter: p.

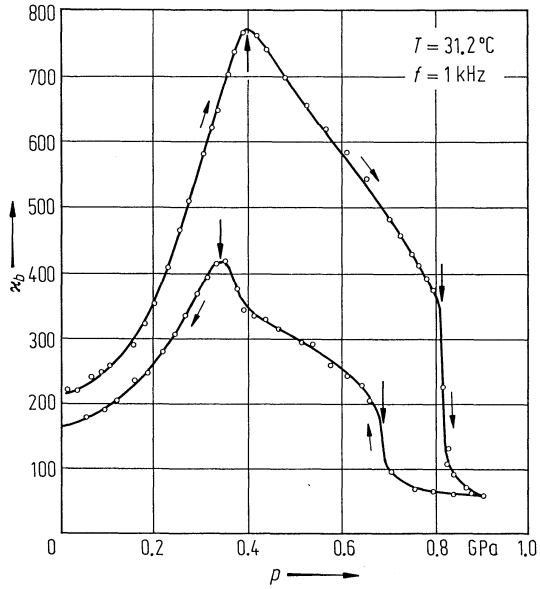

Fig. 33A-2-020. RbD_2PO_4 (monoclinic). κ_b vs. p at 31.2 °C [83Ges].

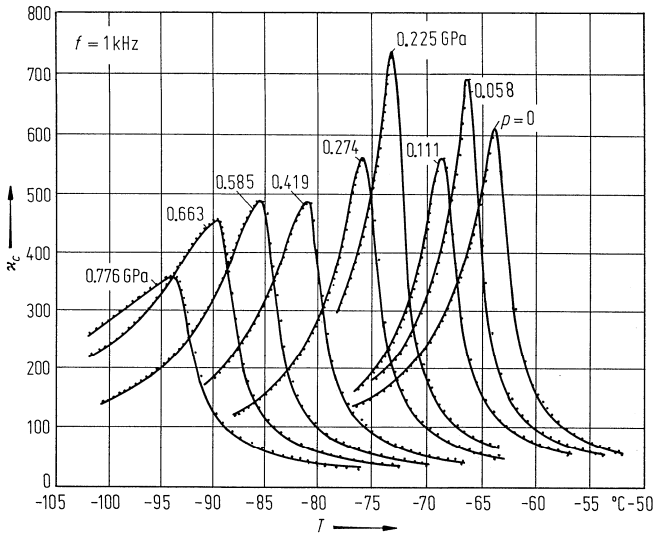

Fig. 33A-2-021. RbD_2PO_4 (tetragonal). κ_c vs. T [83Ges]. Parameter: p.

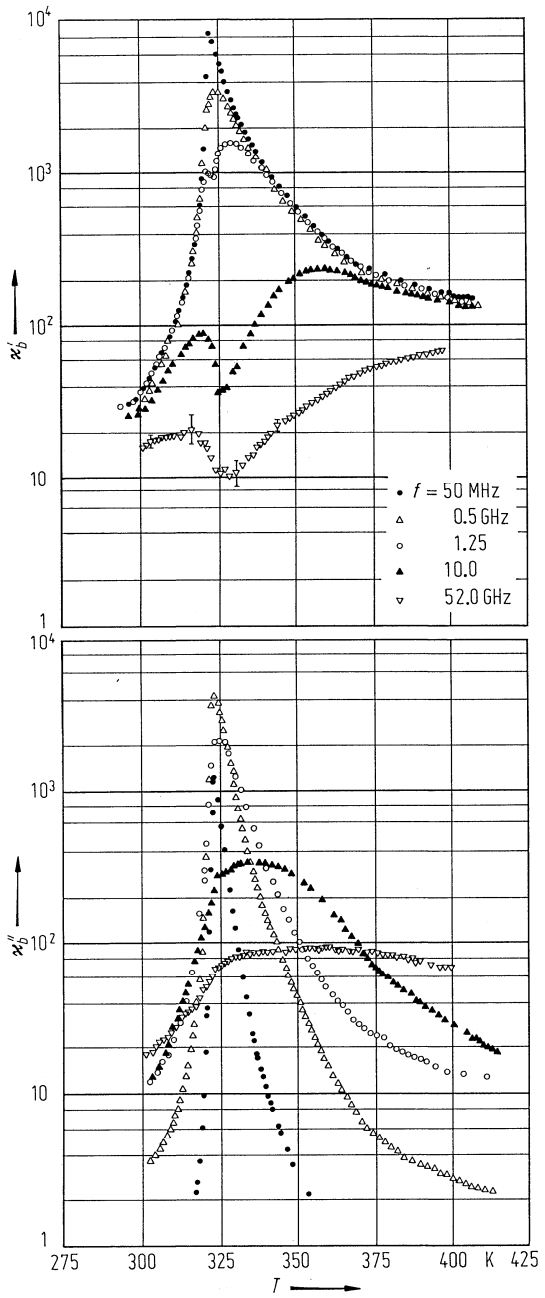

Fig. 33A-2-022. RbD_2PO_4 (monoclinic). κ_b', κ_b'' vs. T [87Miz]. Parameter: f.

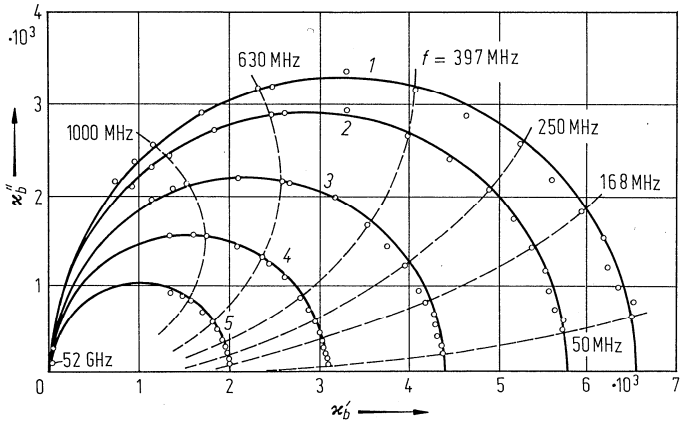

Fig. 33A-2-023. RbD_2PO_4 (monoclinic). κ_b' vs. κ_b'' (Cole-Cole diagram) [87Miz]. Parameter: $T - \Theta_{II'-II'}$. *1*: 1.5 K, *2*: 2.5 K, *3*: 4 K, *4*: 6 K, *5*: 10 K.

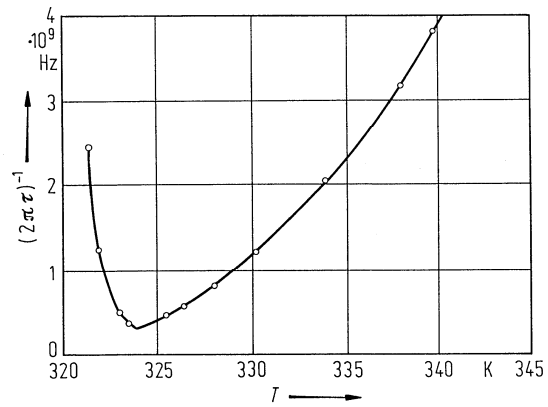

Fig. 33A-2-024. RbD_2PO_4 (monoclinic). $(2\pi\tau)^{-1}$ vs. T [87Miz]. τ: relaxation time of dielectric dispersion.

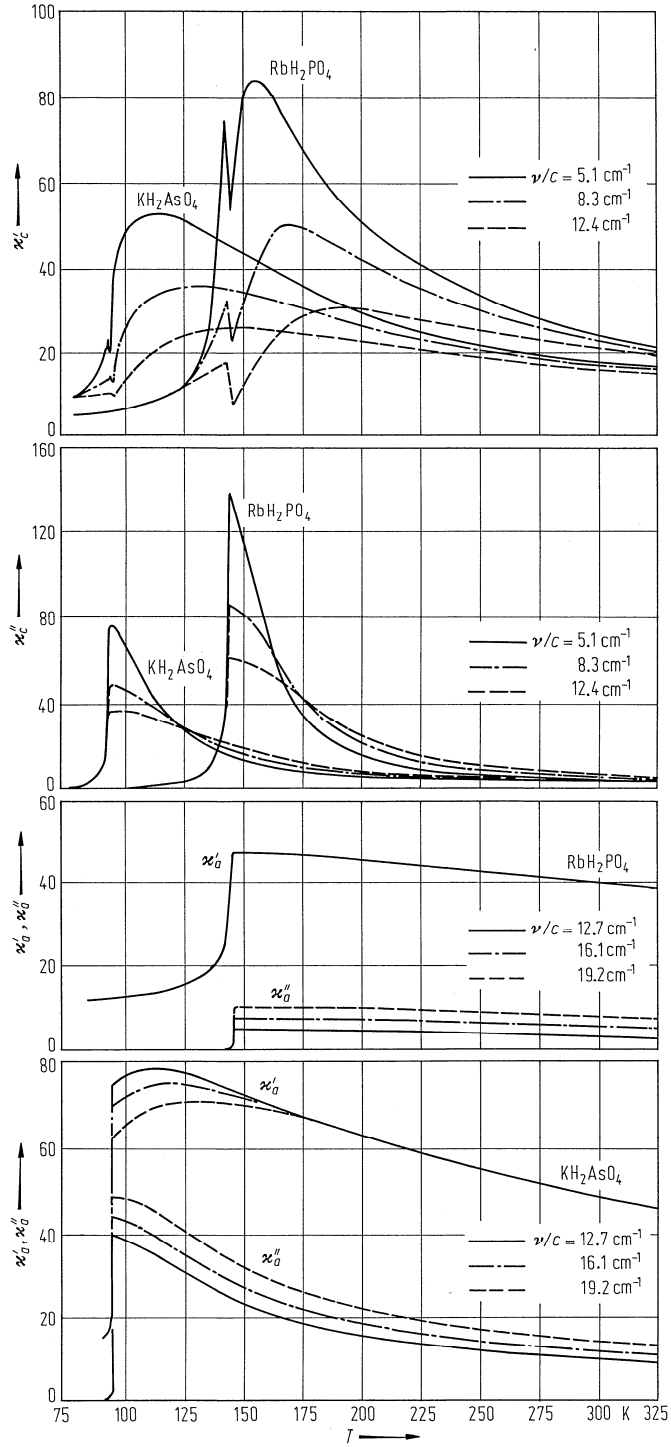

Fig. 33A-2-025. RbH_2PO_4 (RDP), KH_2AsO_4 (KDA). κ_c', κ_c'' and κ_a', κ_a'' vs. T in far-infrared region [79Vol]. Paramter: ν/c.

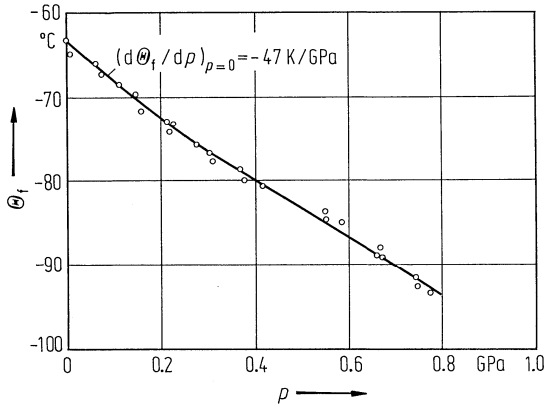

Fig. 33A-2-026. RbD_2PO_4 (tetragonal). Θ_f vs. p [83Ges].

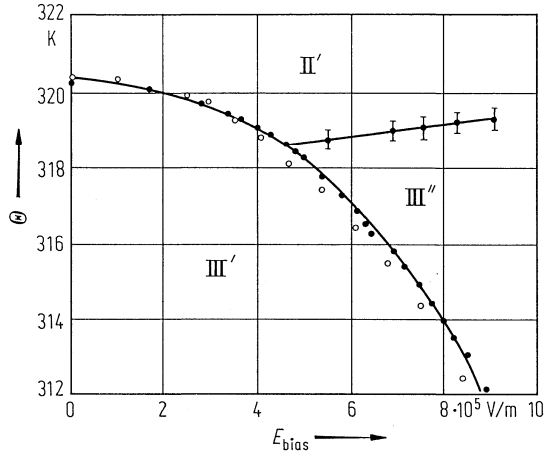

Fig. 33A-2-027. RbD_2PO_4 (monoclinic). Θ vs. E_{bias} [85Bar]. Full circles: dielectric measurement, open circles: birefringence measurement.

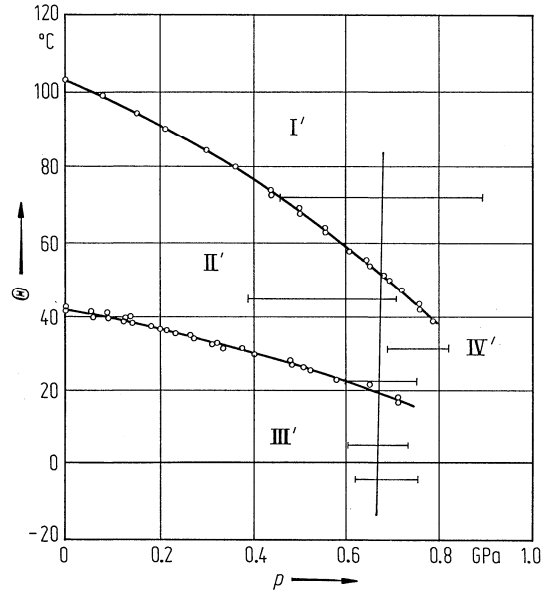

Fig. 33A-2-028. RbD_2PO_4 (monoclinic). Θ vs. p [83Ges].

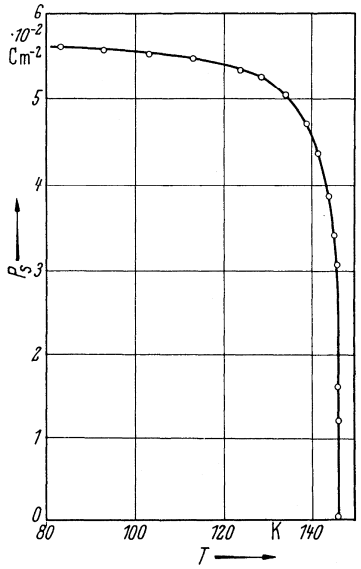

Fig. 33A-2-029. RbH_2PO_4 (RDP). P_s vs. T [50Bec].

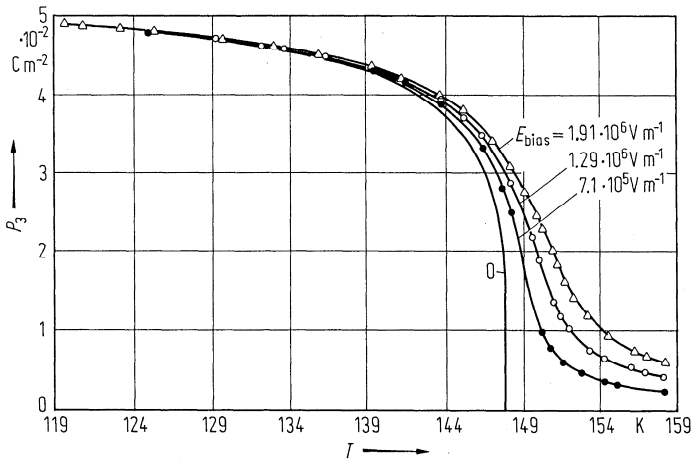

Fig. 33A-2-030. RbH_2PO_4 (RDP). P_3 vs. T [77Cha]. Parameter: E_{bias}. P_3: Polarization along c axis.

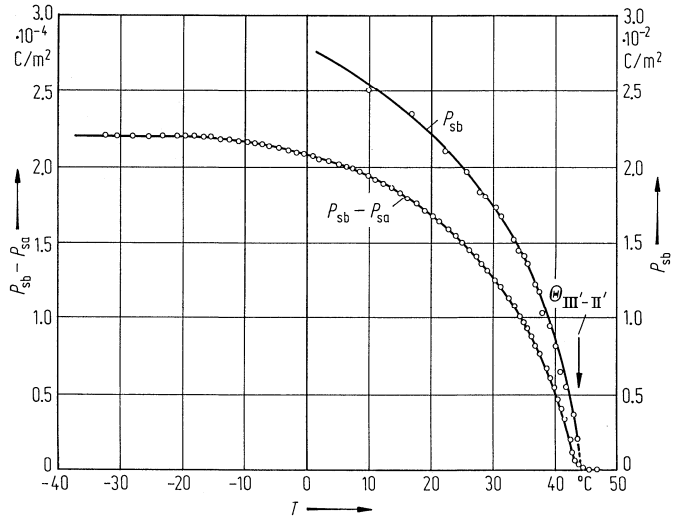

Fig. 33A-2-031. RbD_2PO_4 (monoclinic). $P_{sb} - P_{sa}$, P_{sb} vs. T [83Osa]. P_{sa}, P_{sb}: sublattice polarizations.

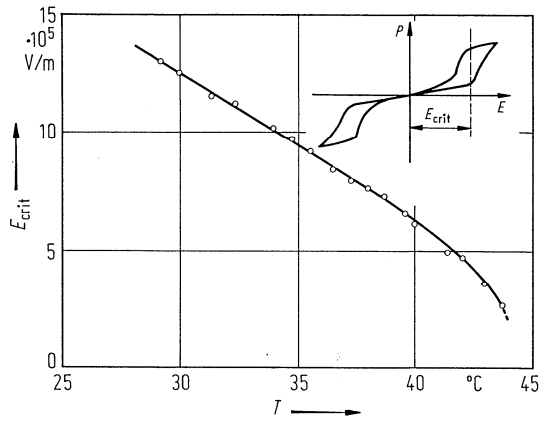

Fig. 33A-2-032. RbD_2PO_4 (monoclinic). E_{crit} vs. T [81Sum]. E_{crit}: critical field (see insert).

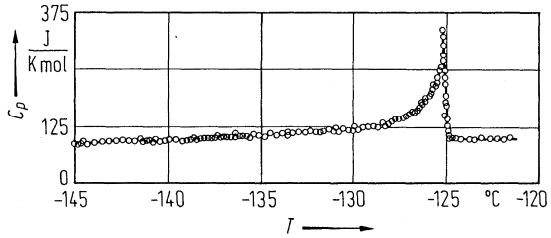

Fig. 33A-2-033. RbH_2PO_4 (RDP). C_p vs. T [68Ami]. C_p: molar heat capacity at constant pressure.

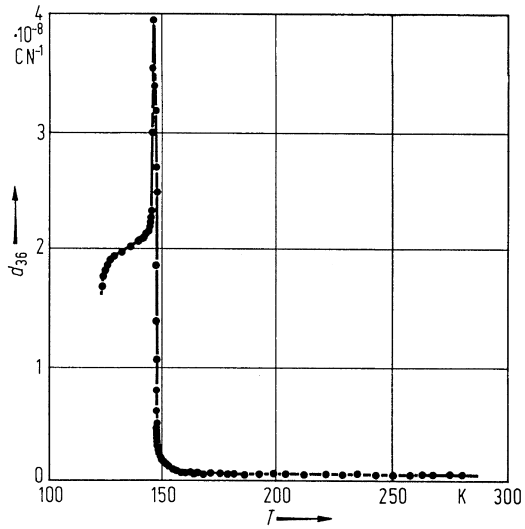

Fig. 33A-2-034. RbH_2PO_4 (RDP). d_{36} vs. T [71Pie].

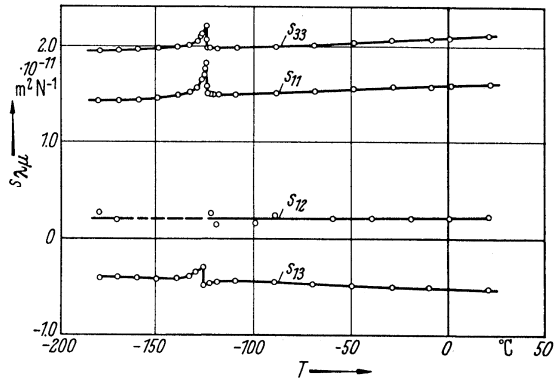

Fig. 33A-2-035. RbH_2PO_4 (RDP). $s_{\lambda\mu}$ vs. T [66Mna].

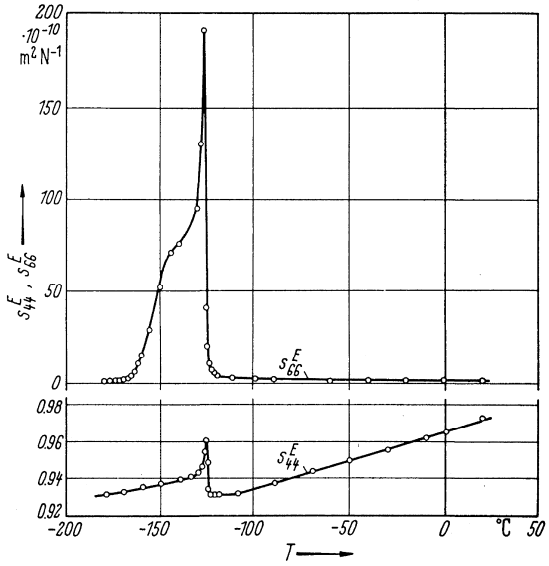

Fig. 33A-2-036. RbH_2PO_4 (RDP). $s_{44}^{\boldsymbol{E}}, s_{66}^{\boldsymbol{E}}$ vs. T [66Mna].

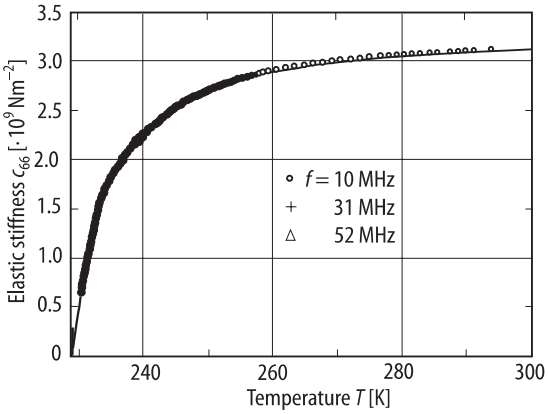

Fig. 33A-2-037. $RH_{2(1-x)}D_{2x}PO_4$ (x = 0.87, tetragonal). c_{66} vs. T [90HuZ]. Parameter: f.

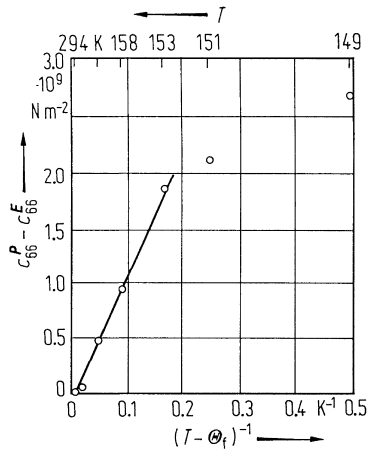

Fig. 33A-2-038. RbH_2PO_4 (RDP). $c_{66}^{P} - c_{66}^{E}$ vs. $(T - \Theta_f)^{-1}$ [71Hau]. $c_{66}^{P} - c_{66}^{E}$: elastic stiffness obtained from Brillouin scattering.

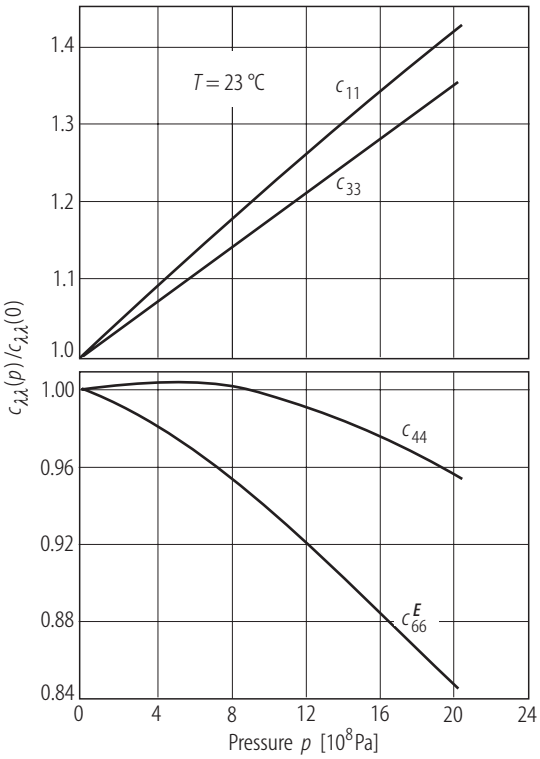

Fig. 33A-2-039. RbD_2PO_4 (DRDP). $c_{\lambda\lambda}(p)/c_{\lambda\lambda}(0)$ vs. p [76Fri]. $c_{\lambda\lambda}(p)$: elastic stiffness under hydrostatic pressure p.

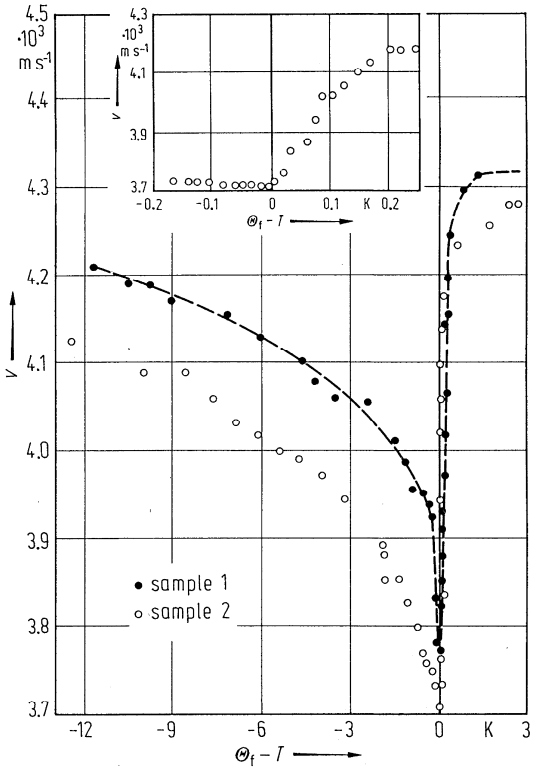

Fig. 33A-2-040. RbH_2PO_4 (RDP). v vs. $\Theta_f - T$ [78Sin]. v: longitudinal sound velocity propagating along c axis. $f = 8$ MHz.

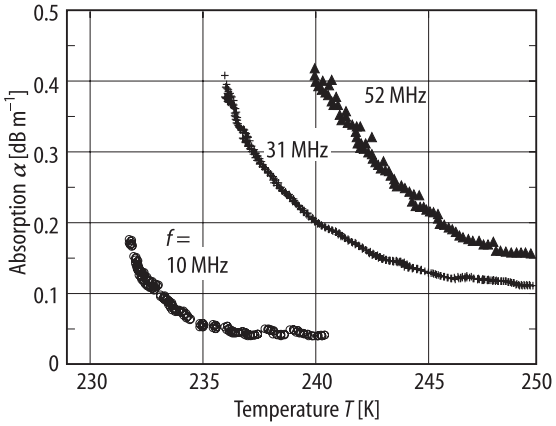

Fig. 33A-2-041. $RH_{2(1-x)}D_{2x}PO_4$ (x = 0.87, tetragonal). α vs. T [90HuZ]. Parameter: f. α: ultrasonic absorption coefficient of the c_{66} mode.

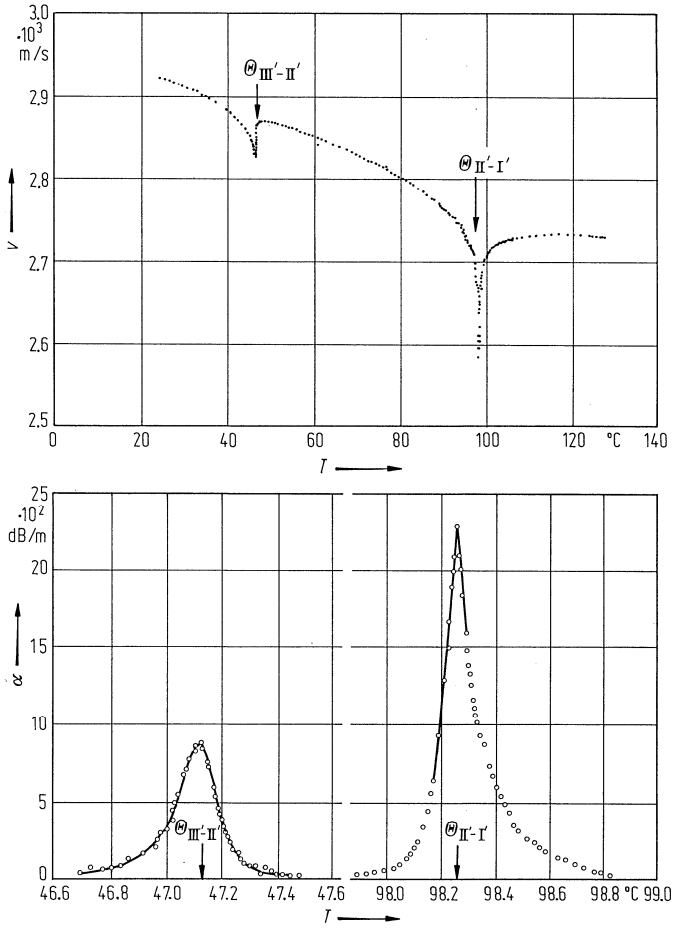

Fig. 33A-2-042. RbD_2PO_4 (monoclinic). υ, α vs. T [86Yak]. υ, α: velocity and attenuation of longitudinal elastic wave propagating along b direction.

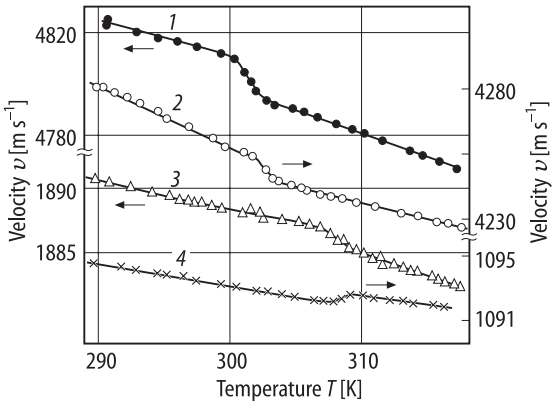

Fig. 33A-2-043. $Rb(H_{0.5}D_{0.5})_2PO_4$ (tetragonal). υ vs. T [80Res]. υ: velocity of elastic wave at 30 MHz. *1*: longitudinal wave propagating along [100] direction; *2*: longitudinal wave propagating along [001] direction; *3*: transverse wave propagating along [001] direction with the shift parallel to [100]; *4*: transverse wave propagating along [100] direction with the shift parallel to [010].

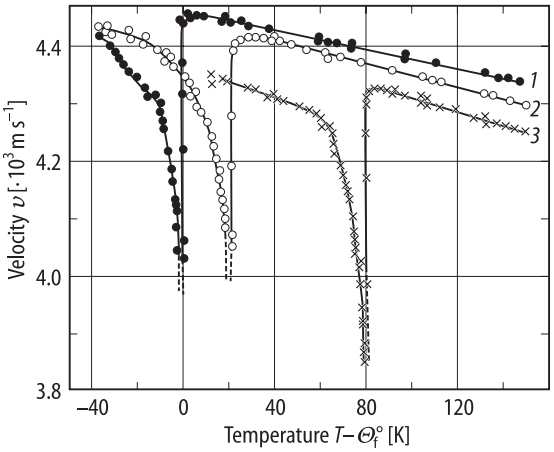

Fig. 33A-2-044. $RbH_{2(1-x)}D_{2x}PO_4$. v vs. $T - \Theta_f^0$ [72Mis]. Parameter: x. v: velocity of longitudinal elastic wave propagating along *c* axis. f = 30 MHz. Θ_f^0 : Θ_f at x = 0. *1*: x = 0, *2*: x = 0.2, *3*: x = 0.8.

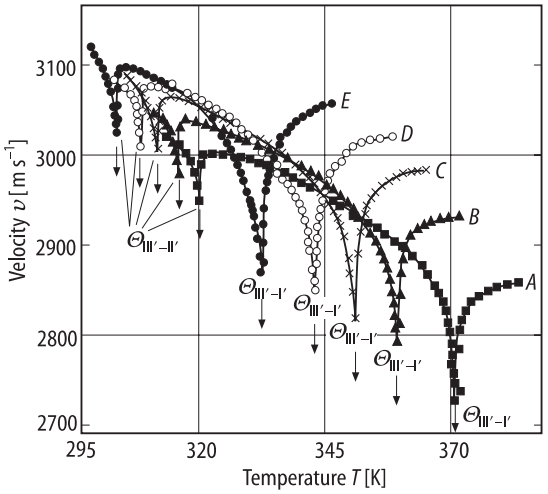

Fig. 33A-2-045. RbD_2PO_4 (monoclinic). v vs. T [94Kit]. Parameter: p. v: velocity of longitudinal elastic wave propagating along [010] direction. f = 10 MHz. *A*: p = 0.1 MPa, *B*: 175 MPa, *C*: 295 MPa, *D*: 385 MPa, *E*: 495 MPa.

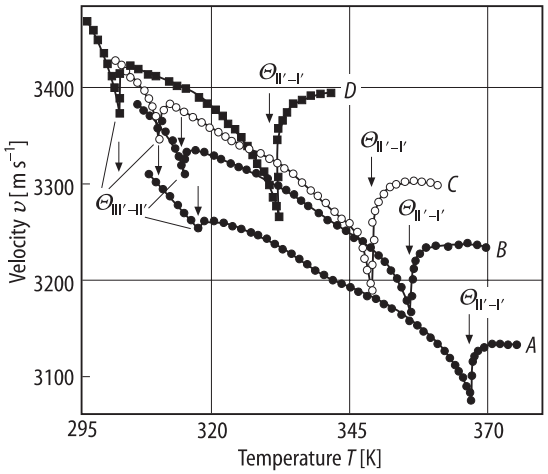

Fig. 33A-2-046. RbD_2PO_4 (monoclinic). v vs. T [94Kit]. Parameter: p. v: velocity of quasi-longitudinal elastic wave propagating normal to the *bc* plane. f = 10 MHz. *A*: p = 45 MPa, *B*: 205 MPa, *C*: 315 MPa, *D*: 495 MPa.

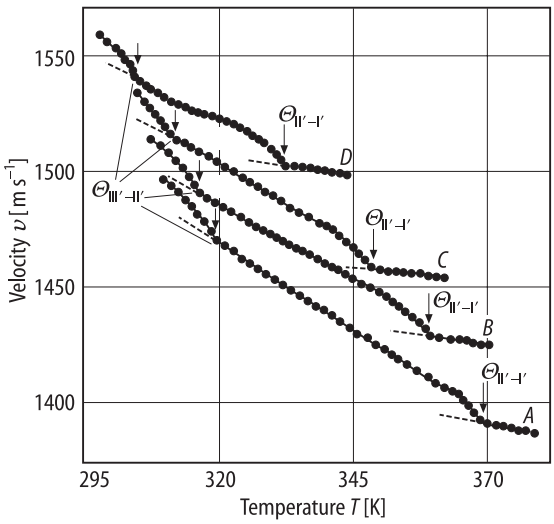

Fig. 33A-2-047. RbD_2PO_4 (monoclinic). v vs. T [94Kit]. Parameter: p. v: velocity of transverse elastic wave propagating along the *b* axis with the shift in *ac* plane. f = 10 MHz. *A*: p = 0.1 MPa, *B*: 155 MPa, *C*: 295 MPa, *D*: 495 MPa.

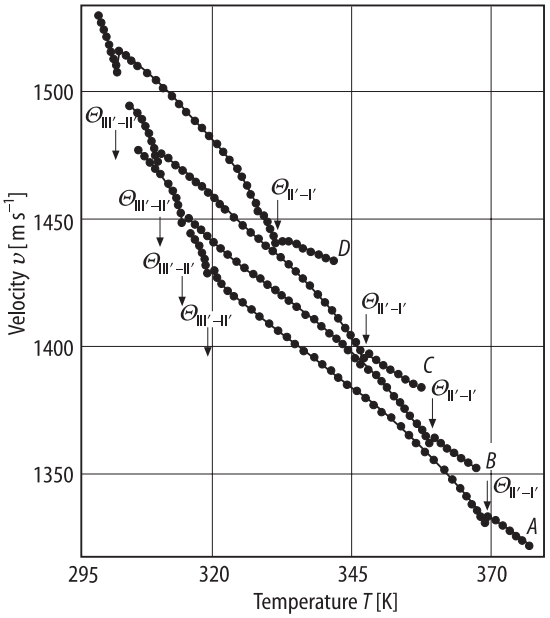

Fig. 33A-2-048. RbD_2PO_4 (monoclinic). v vs. T [94Kit]. Parameter: p. v: velocity of quasi-transverse elastic wave propagating along the normal to the *bc* plane with the shift parallel to [001] direction. f = 10 MHz. *A*: p = 0.1 MPa, *B*: 165 MPa, *C*: 315 MPa, *D*: 495 MPa.

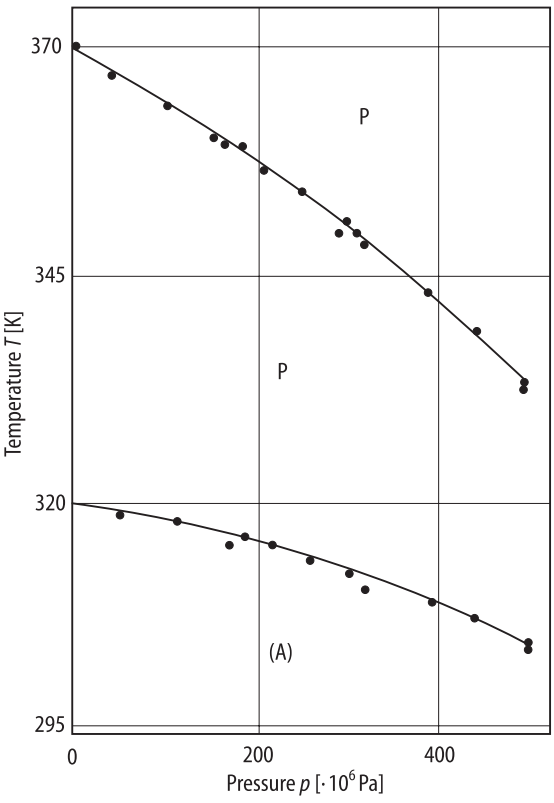

Fig. 33A-2-049. RbD_2PO_4 (monoclinic). p–T phase diagram determined by ultrasonic velocity [94Kit].

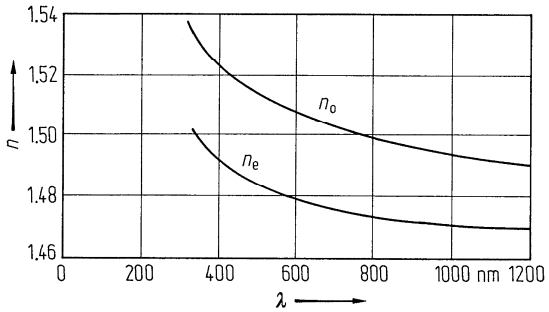

Fig. 33A-2-050. RbH_2PO_4 (RDP). n vs. λ at RT [70Gol].

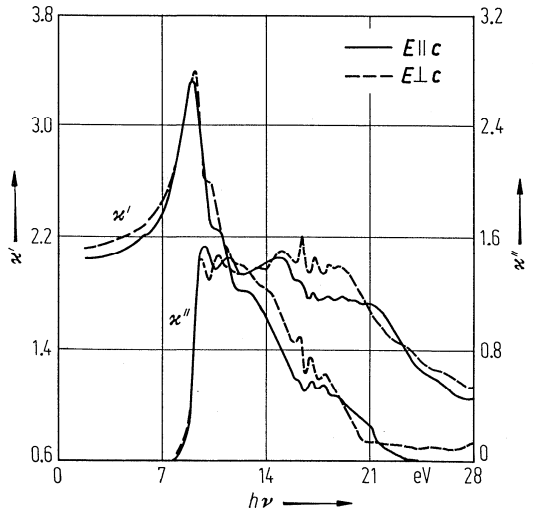

Fig. 33A-2-051. RbH_2PO_4 (RDP). κ', κ'' vs. $h\nu$ in vacuum ultraviolet region at RT [85Mat]. κ': real part, and κ'': imaginary part of complex dielectric constant.

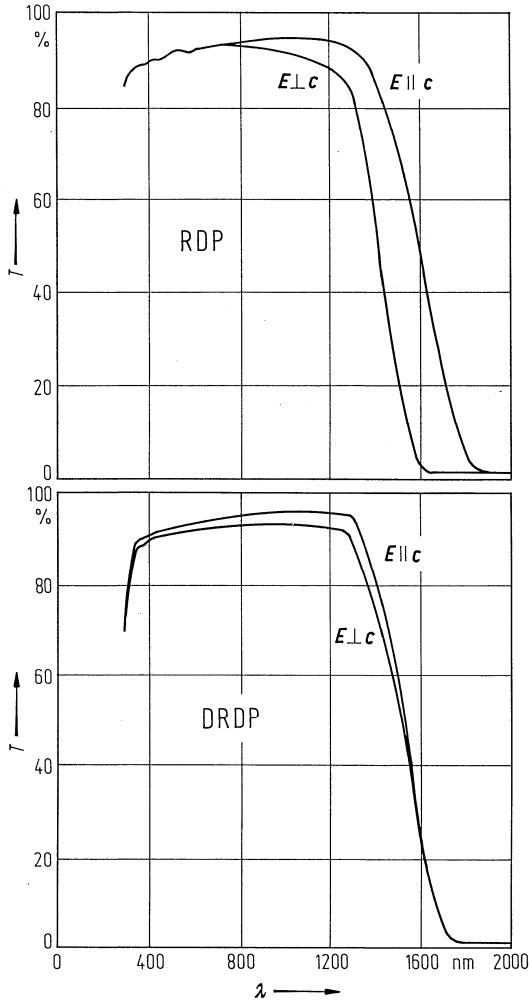

Fig. 33A-2-052. RbH_2PO_4 (RDP), RbD_2PO_4 (DRDP) (tetragonal). T vs. λ [87Eim]. T: transmission. Sample thickness: 11 mm.

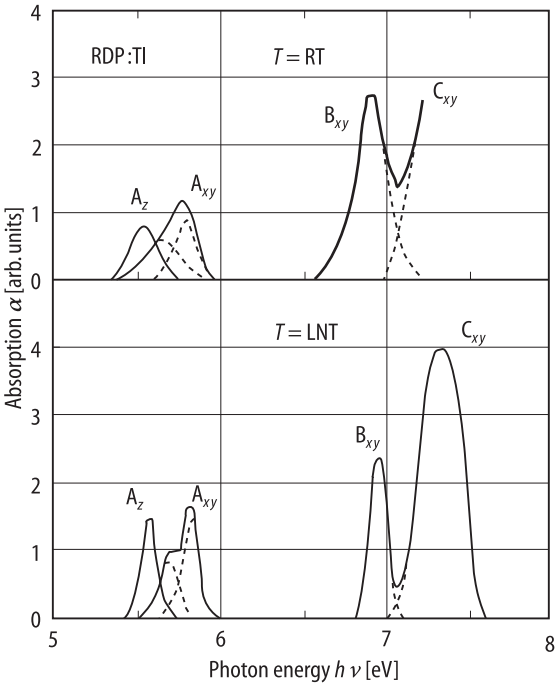

Fig. 33A-2-053. RbH_2PO_4:Tl. α vs. $h\nu$ [94Fuj]. α: absorption of light polarized parallel (A_z) or perpendicular (A_{xy}, B_{xy}, C_{xy}) to the z axis. A, B, C stand for corresponding absorption bands A, B, C of Tl^+ centers in alkali halides, respectively.

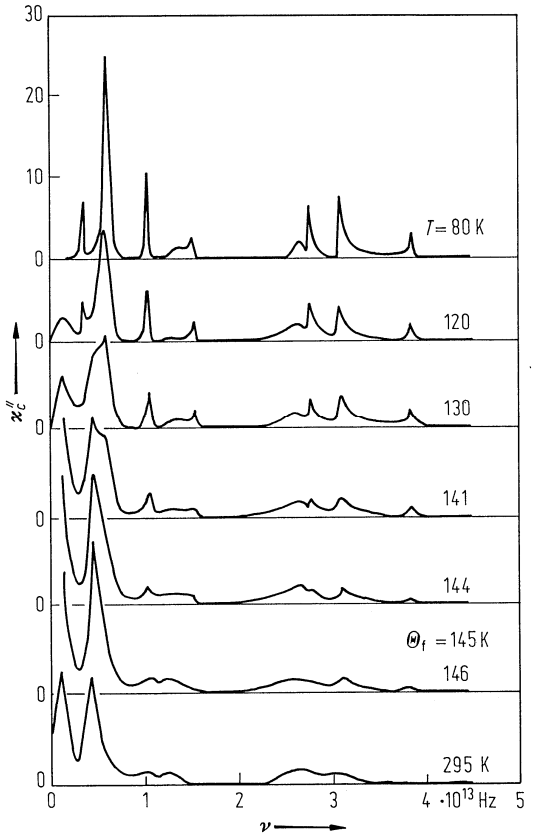

Fig. 33A-2-054. RbH_2PO_4 (RDP). κ_c'' vs. ν [88Sim]. Parameter: *T*. ν: frequency of far-infrared radiation.

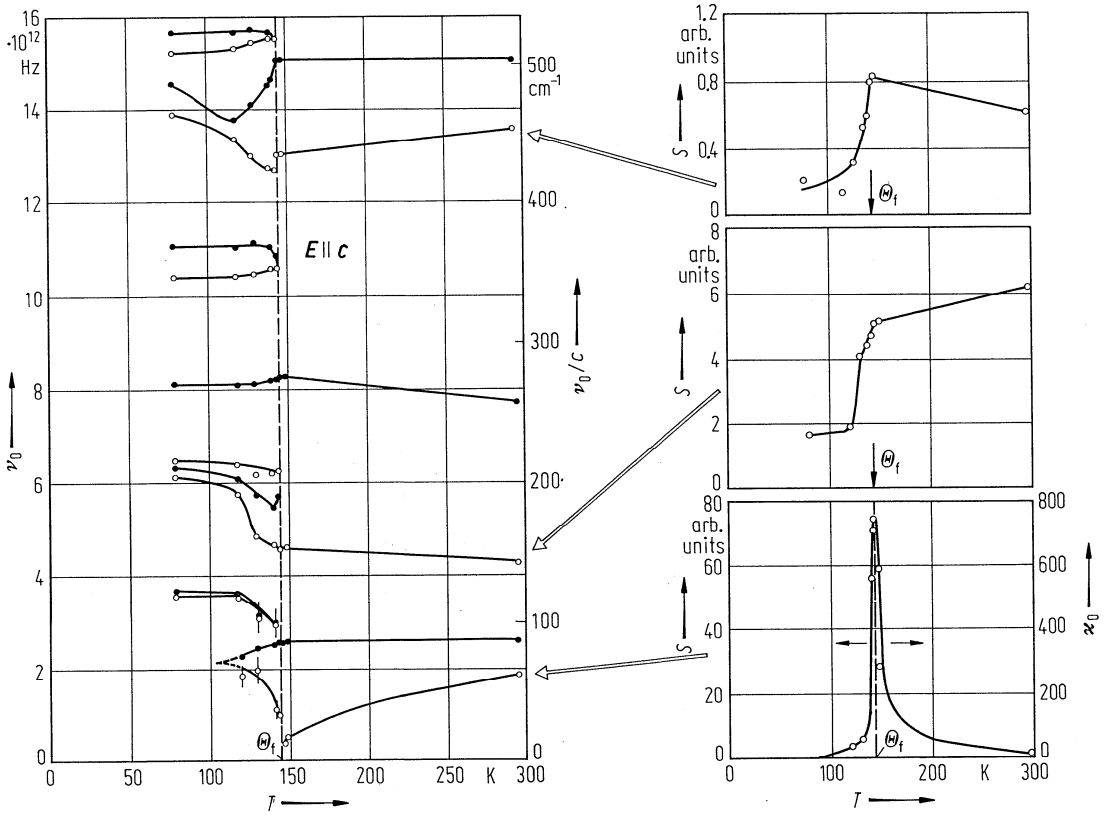

Fig. 33A-2-055. RbH_2PO_4 (RDP). ν_0 vs. T [85Sim]. ν_0: mode frequencies obtained from far-infrared reflection spectra. Open circle: TO mode, full circle: LO mode. Right hand figures show the oscillator strengths S of the TO modes vs. T. κ_0: static dielectric constant.

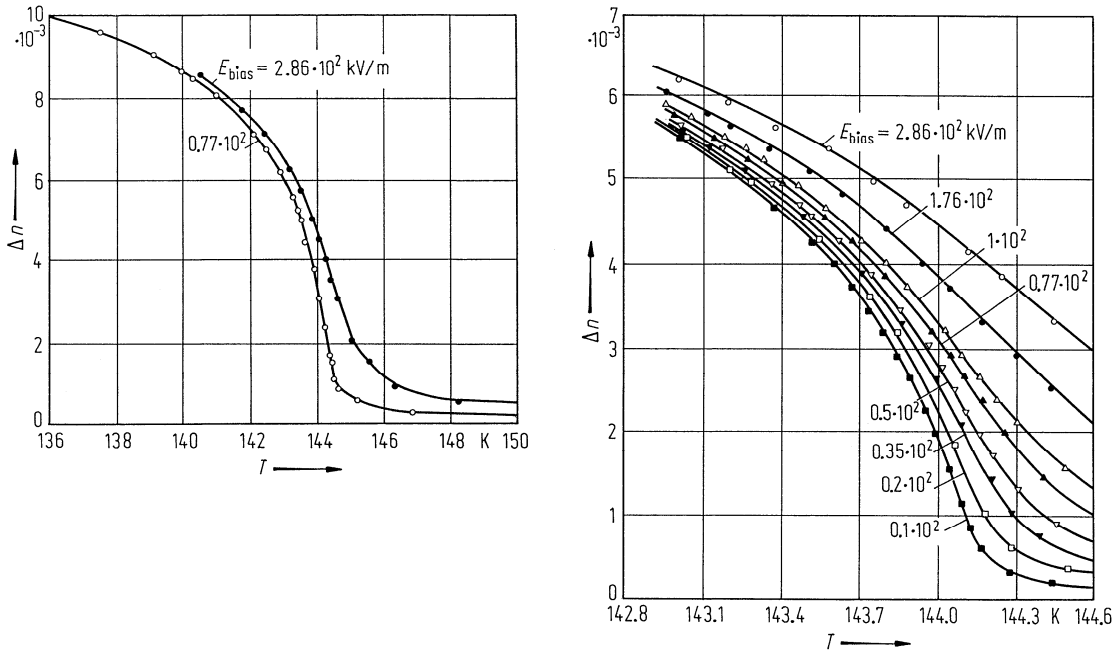

Fig. 33A-2-056. RbH_2PO_4 (RDP). Δn vs. T [80Tro]. Parameter: E_{bias}. $\Delta n = n_a - n_b$. $\lambda = 632.8$ nm.

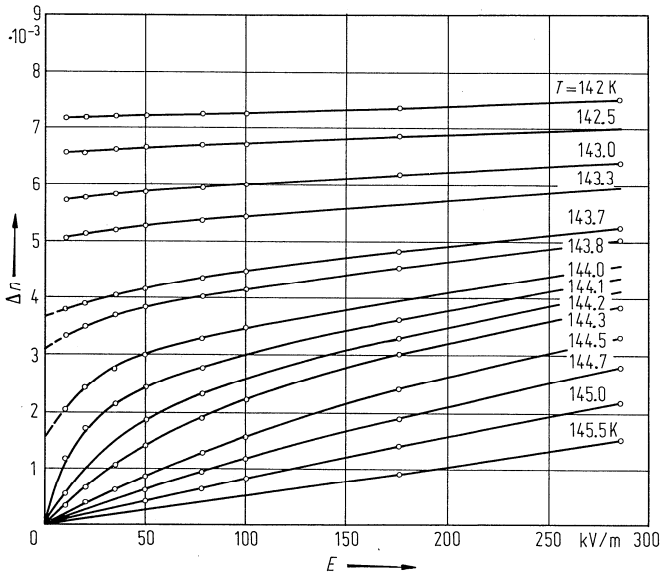

Fig. 33A-2-057. RbH_2PO_4 (RDP). Δn vs. E [80Tro]. Parameter: T. $\Delta n = n_a - n_b$. E: external dc electric field. $\lambda = 632.8$ nm.

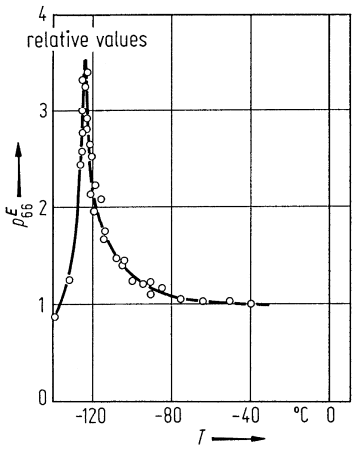

Fig. 33A-2-058. RbH_2PO_4 (RDP). p_{66}^{E} vs. T [71Hau]. p_{66}^{E} : piezooptic constant obtained from Brillouin scattering intensity.

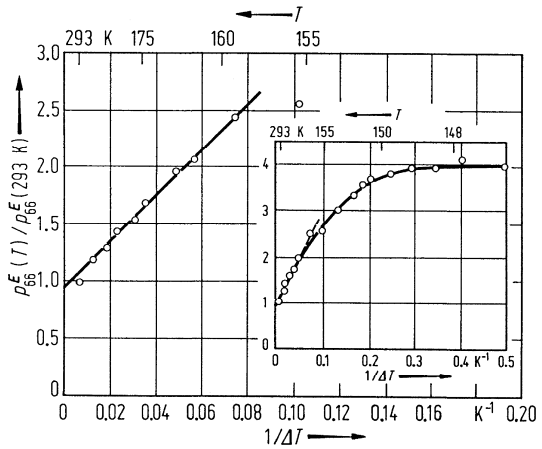

Fig. 33A-2-059. RbH_2PO_4 (RDP). $p_{66}^{E}(T)$ / p_{66}^{E} (293 K) vs. $1/\Delta T$ [72Hau]. $p_{66}^{E}(T)$: piezooptic constant for constant E at T obtained from Brillouin scattering. ΔT: $T - \Theta_f$.

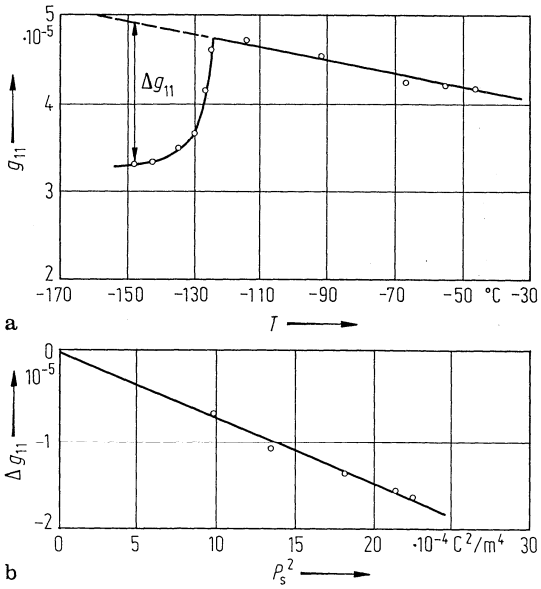

Fig. 33A-2-060. RbH_2PO_4 (RDP). (**a**) g_{11} vs. T, (**b**) Δg_{11} vs. P_s^2 [86Vlo]. g_{11}: gyration tensor component. $\lambda = 632.8$ nm.

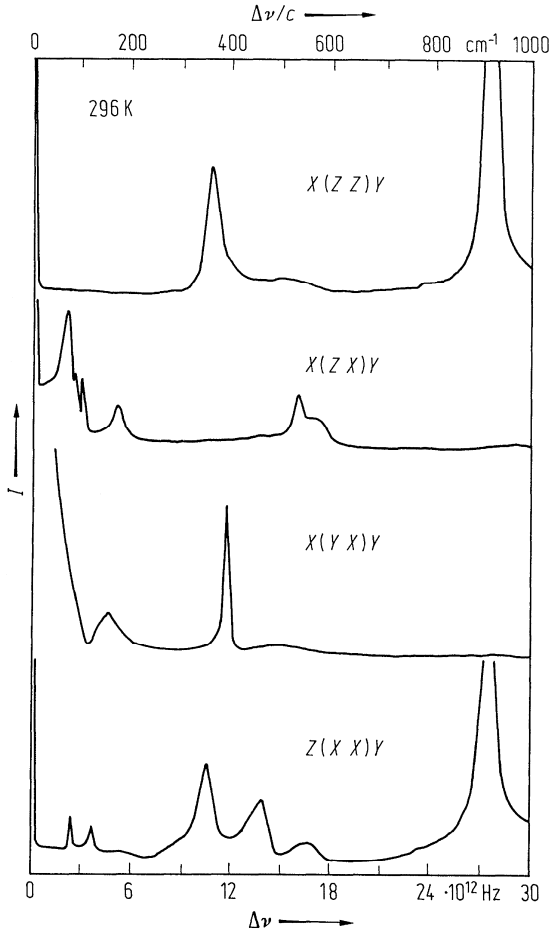

Fig. 33A-2-061. RbH_2PO_4 (RDP). I vs. $\Delta\nu$ [73Pee]. T = 296 K. I: Raman scattering intensity in various scattering geometries.

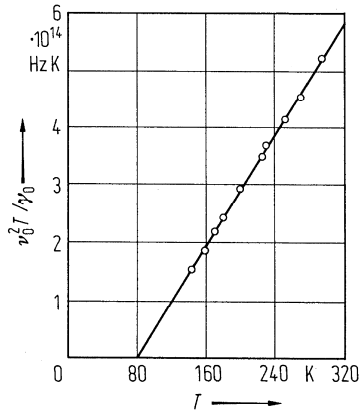

Fig. 33A-2-062. RbH_2PO_4 (RDP). $\nu_0^2 T / \gamma_0$ vs. T [73Pee]. ν_0, γ_0: characteristic frequency and damping constant, respectively, of the soft mode obtained from Raman spectrum.

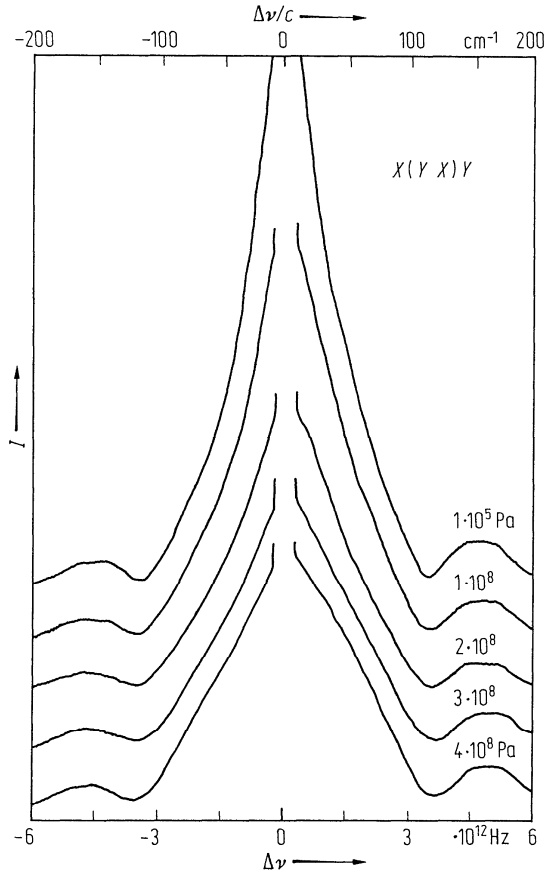

Fig. 33A-2-063. RbH_2PO_4 (RDP). I vs. $\Delta\nu$ [73Pee]. I: Raman scattering intensity at 296 K in a scattering geometry of $X(YX)Y$. Parameter: p.

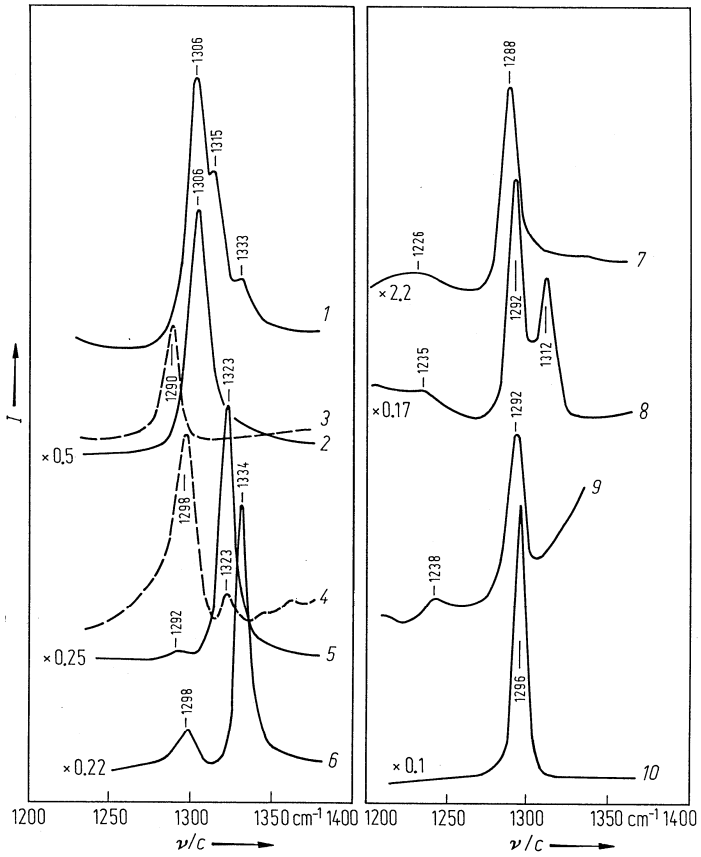

Fig. 33A-2-064. RbH_2PO_4 (RDP). *I* vs. *ν/c* [84Dav]. *I*: Raman scattering intensity at 7 K. Scattering geometry: *1*: *Y*(*XZ*)*Y*; *2*: *Z*(*X′Z*)*Y′*; *3*: *Z*(*Y′Z*)*Y′*; *4*: *Z*(*Y′Z*)*X′*; *5*: *Z*(*X′Z*)*X′*; *6*: *X*(*YZ*)*Y*; *7*: *Y*(*ZZ*)*X*; *8*: *Z*(*X′X′*)*Y′*; *9*: *Z*(*Y′Y′*)*X′*; *10*: *X′*(*Y′X′*)*Y′*. *X*, *Y*, *Z*: paraelectric axes; *X′*, *Y′*, *Z′*: ferroelectric axes.

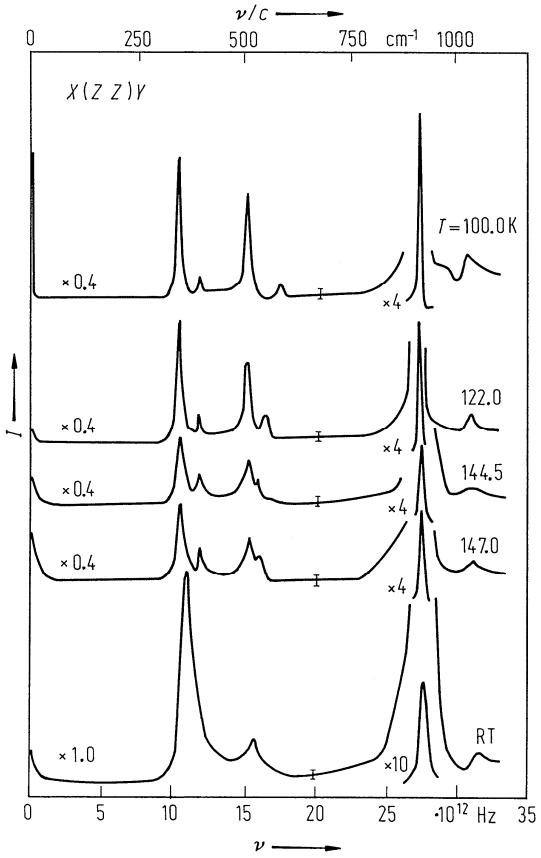

Fig. 33A-2-065. RbH_2PO_4 (RDP). I vs. ν [84Mar]. Parameter: T. I: Raman intensity. Scattering geometry: $X(ZZ)Y$.

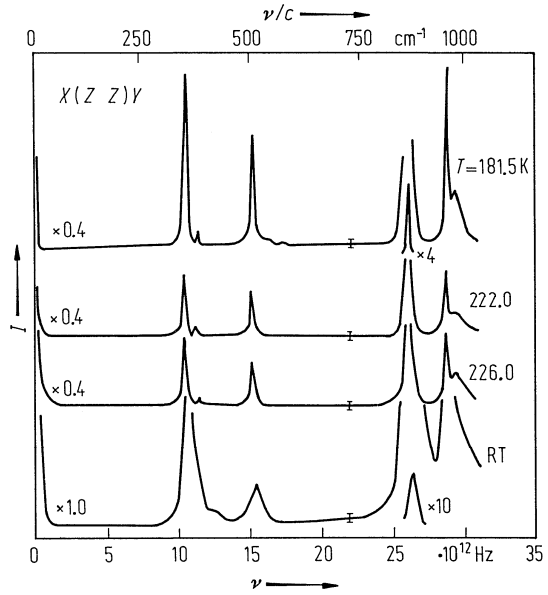

Fig. 33A-2-066. RbD_2PO_4 (DRDP, tetragonal). I vs. ν [84Mar]. Parameter: T. I: Raman intensity. Scattering geometry: $X(ZZ)Y$.

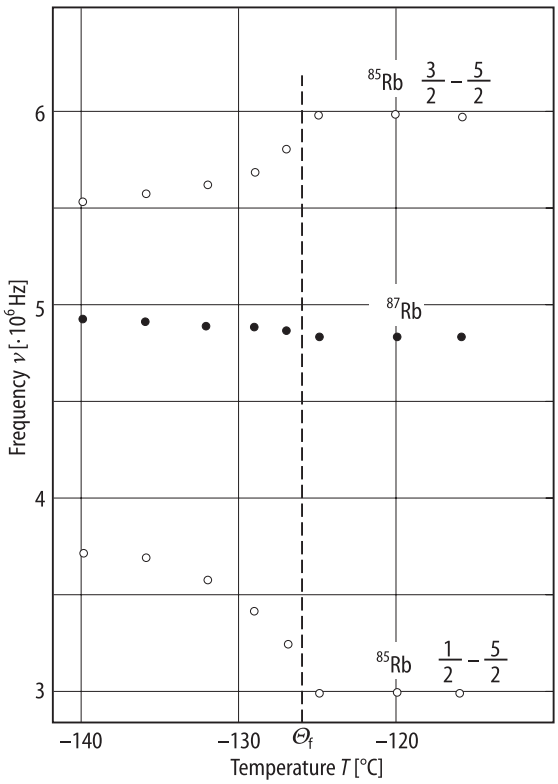

Fig. 33A-2-067. RbH_2PO_4 (RDP). ν vs. T [90Sel]. ν: ^{85}Rb and ^{87}Rb NQR frequencies.

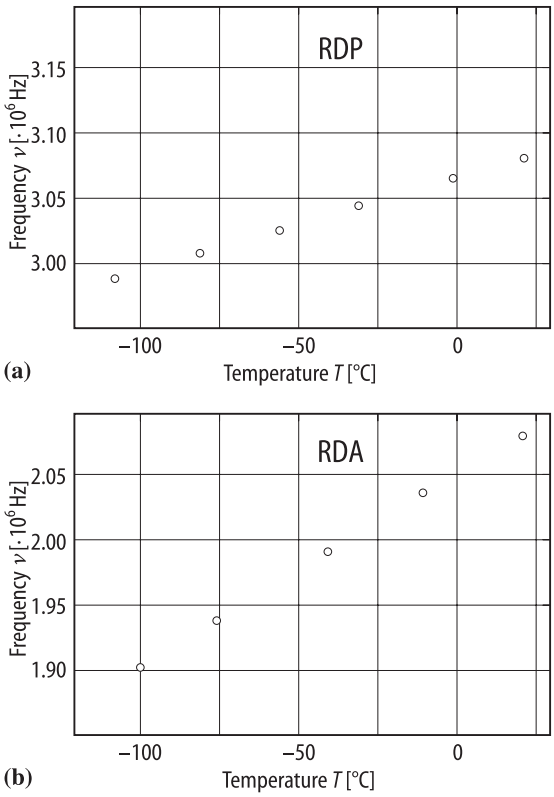

Fig. 33A-2-068. (**a**) RbH_2PO_4 (RDP), (**b**) RbH_2AsO_4 (RDA). ν vs. T [94Sel]. ν: ^{85}Rb NQR frequency of 1/2 ↔ 2/3 transition.

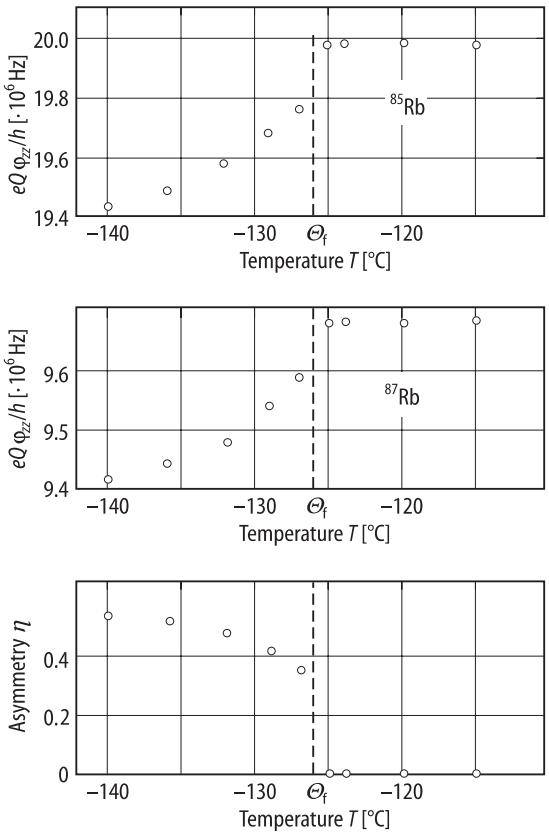

Fig. 33A-2-069. RbH_2PO_4 (RDP). $eQ\phi_{zz}/h$, η vs. T [90Sel]. $eQ\phi_{zz}/h$: component of quadrupole coupling tensor for ^{85}Rb or ^{87}Rb. η: asymmetry parameter at Rb site.

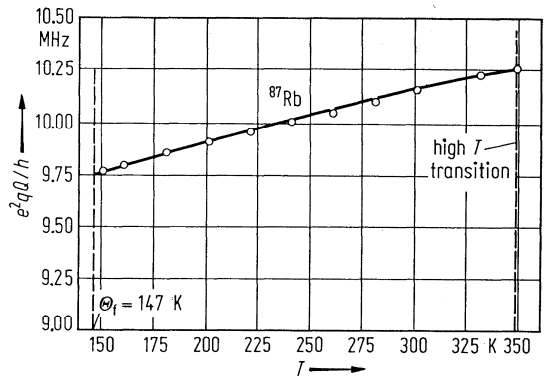

Fig. 33A-2-070. RbH_2PO_4 (RDP). e^2qQ/h for ^{87}Rb vs. T [70Bli].

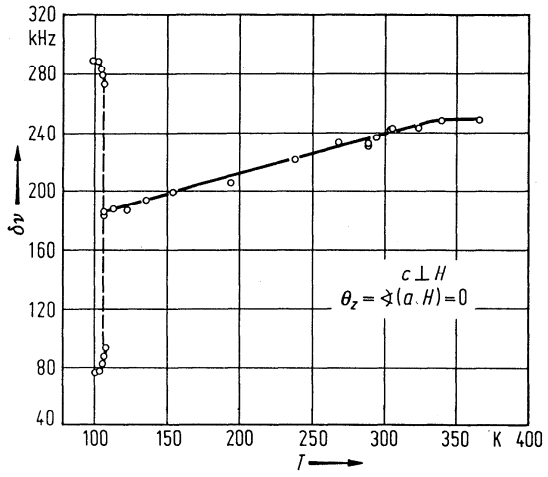

Fig. 33A-2-071. RbH_2PO_4 (RDP). $\delta\nu$ vs. T [69Bli1]. $\delta\nu$: second order shift of the $1/2 \rightarrow -1/2$ transition of ^{87}Rb. $\boldsymbol{H} \parallel \boldsymbol{a}$, $\boldsymbol{H} \perp \boldsymbol{c}$, $f = 9.160$ MHz.

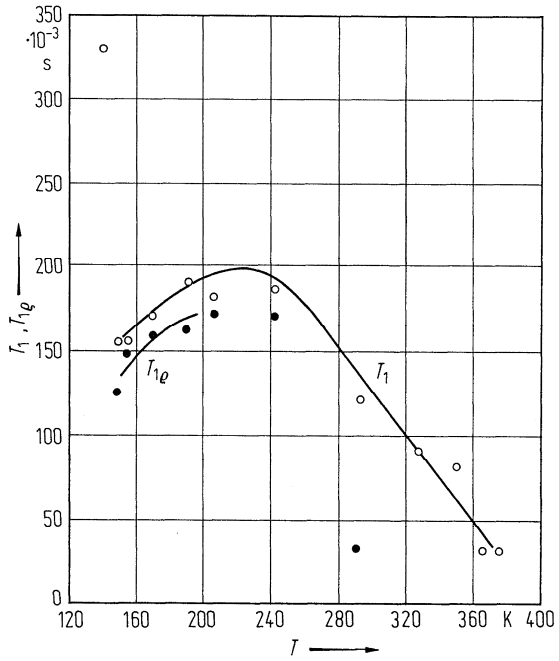

Fig. 33A-2-072. RbH_2PO_4 (RDP). T_1, $T_{1\rho}$ vs. T [75Bli]. Open circles: T_1 of ^{87}Rb; full circles: $T_{1\rho}$ of ^{87}Rb. $H_1 = 3.2 \cdot 10^2$ A m^{-1}. $f = 18$ MHz. $\boldsymbol{H} \perp \boldsymbol{c}$ axis.

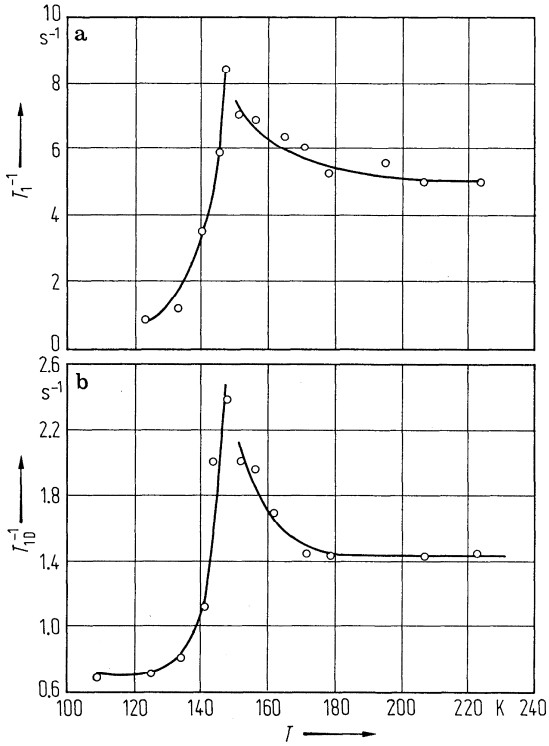

Fig. 33A-2-073. RbH_2PO_4 (RDP). T_1^{-1}, T_{1D}^{-1} vs. T [75Gup]. (**a**) T_1: ^{87}Rb spin lattice relaxation time. (**b**) T_{1D}: ^1H dipolar spin lattice relaxation time.

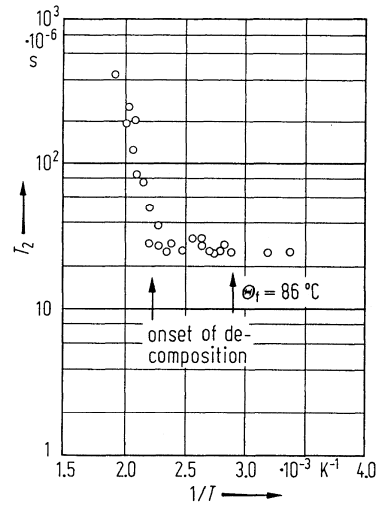

Fig. 33A-2-074. RbH_2PO_4 (RDP). T_2 vs. l/T [69Bli1]. T_2: proton spin-spin relaxation time.

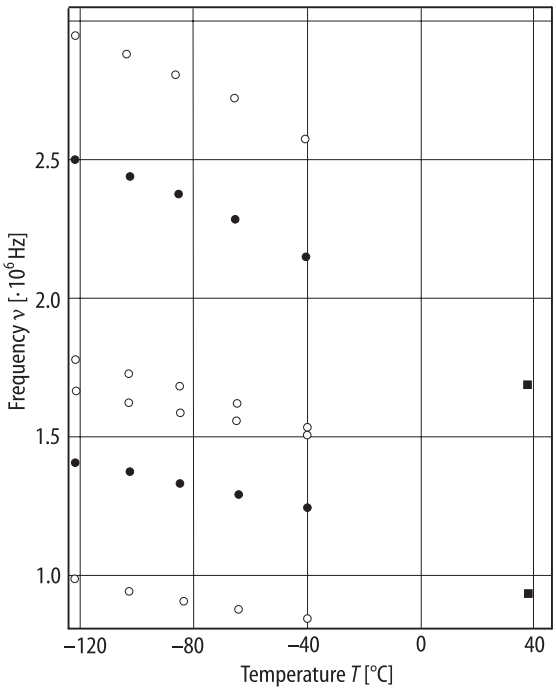

Fig. 33A-2-075. RbH_2PO_4 (monoclinic), RbD_2PO_4 (monoclinic). ν vs. T [93Sel]. ν: ^{85}Rb and ^{87}Rb NQR frequencies. Open circle: ^{85}Rb in RbH_2PO_4; full circle: ^{87}Rb in RbH_2PO_4; full square: ^{87}Rb in RbD_2PO_4.

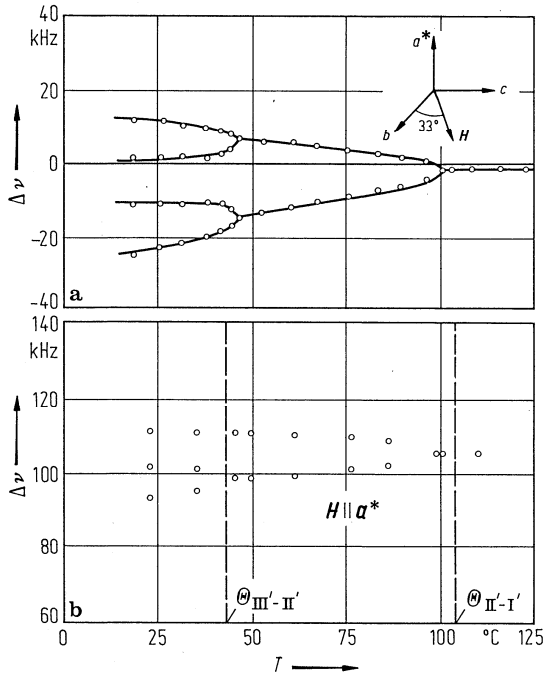

Fig. 33A-2-076. RbD_2PO_4 (monoclinic). $\Delta\nu$ vs. T [84Top]. $\Delta\nu$: quadrupole shift. (**a**) ^{87}Rb 1/2 ↔ – 1/2 transition, ν_L = 26 MHz; $\boldsymbol{H} \perp \boldsymbol{a}$, $\angle \boldsymbol{H} \cdot \boldsymbol{b}$ = 33°. (**b**) ^{2}D line, ν_L = 41.45 MHz; $\boldsymbol{H} \parallel \boldsymbol{a}^*$.

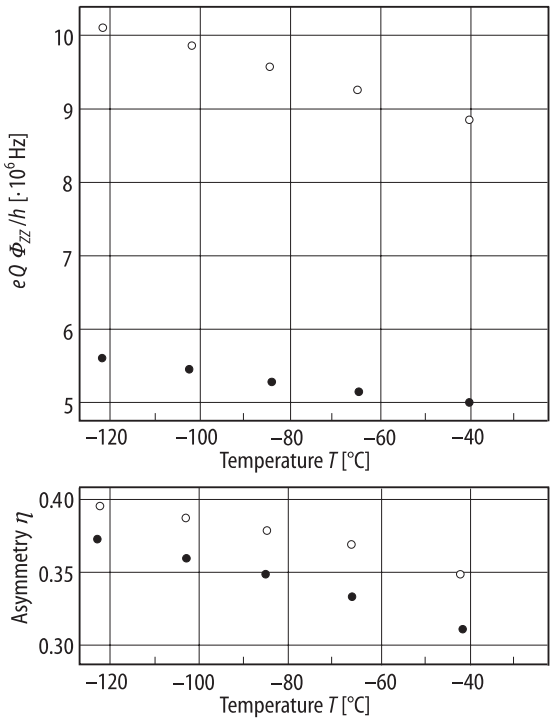

Fig. 33A-2-077. RbH_2PO_4 (supercooled monoclinic). $eQ\phi_{zz}/h$, η vs. T [93Sel]. $eQ\phi_{zz}/h$: component of quadrupole coupling tensor for ^{85}Rb. η: asymmetry parameter. Two nonequivalent Rb sites are indicated by open and solid circles.

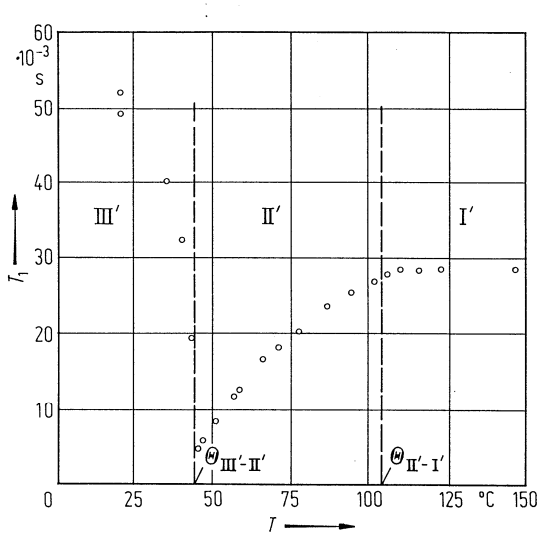

Fig. 33A-2-078. RbD_2PO_4 (monoclinic). T_1 vs. T [84Top]. T_1: ^{87}Rb spin-lattice relaxation time. ν_L = 26 MHz, $\boldsymbol{H} \parallel \boldsymbol{a}^*$.

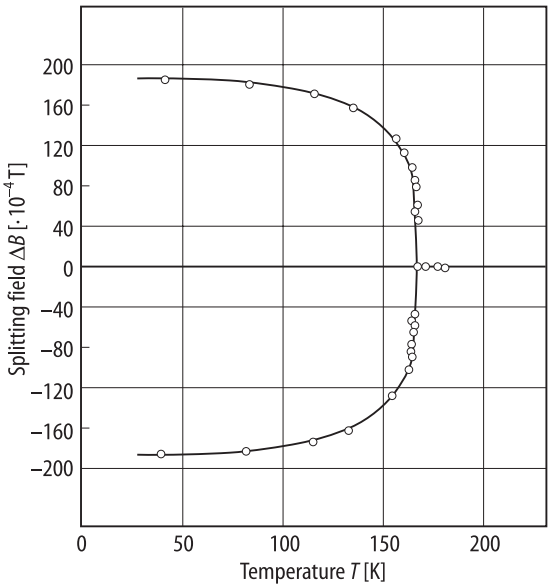

Fig. 33A-2-079. RbH_2PO_4:Tl^{2+}. ΔB vs. T [88Bli]. ΔB: doublet splitting field of Tl^{2+} ESR line. $\boldsymbol{H_0} \perp \boldsymbol{c}$, $\boldsymbol{H_0} \parallel \boldsymbol{a}$, $\boldsymbol{b}$. H_0: external magnetic field.

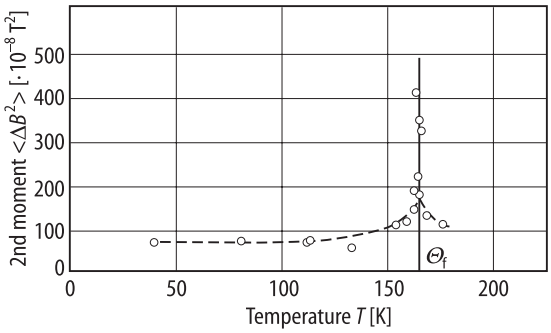

Fig. 33A-2-080. RbH_2PO_4:Tl^{2+}. $\langle \Delta B^{\,2} \rangle$ vs. T [88Bli]. $\langle \Delta B^{\,2} \rangle$: second moment of Tl^{2+} ESR line. $\boldsymbol{H_0} \perp \boldsymbol{c}$, $\boldsymbol{H_0} \parallel \boldsymbol{a}$, $\boldsymbol{b}$. H_0: external magnetic field.

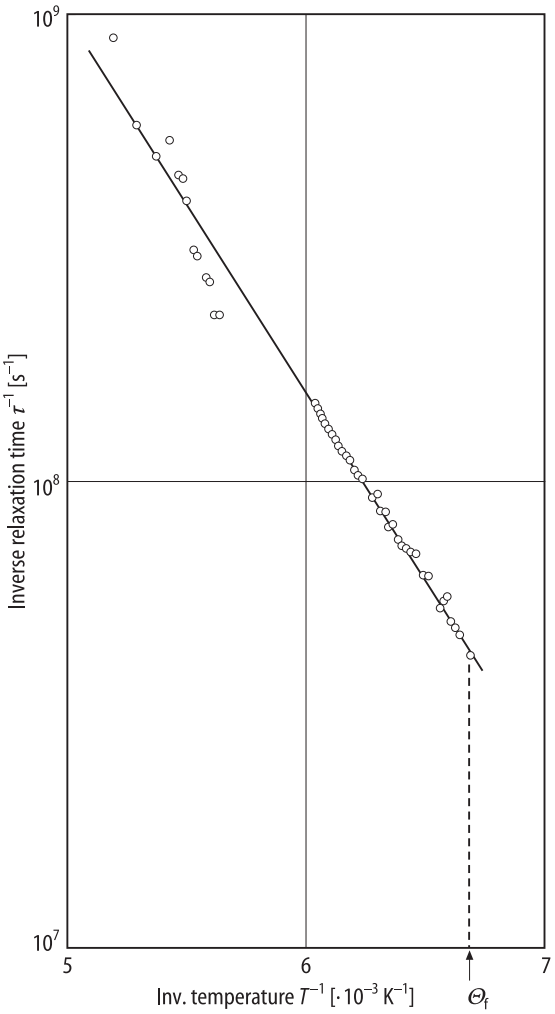

Fig. 33A-2-081. RbH_2PO_4: SeO_4^{3-}. τ^{-1} vs. T^{-1} [90Mat]. τ: inverse of the slow fluctuation rate of Se determined from ESR. The solid line indicates the Arrhenius formula $1/\tau = 1/\tau_0 \exp(-E/kT)$ with $1/\tau_0 = 1.0 \cdot 10^{13}$ Hz, $E = 0.16$ eV.

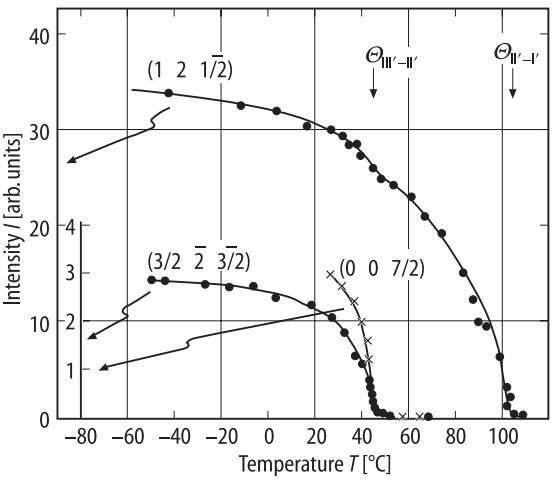

Fig. 33A-2-082. RbD_2PO_4 (monoclinic). I vs. T [83Suz]. I: integrated intensity of X-ray satellite scattering.